A STUDY ON THE POSSIBILITY OF USING THERMALLY-POLED SILICA WAVEGUIDES FOR OPTICAL COMMUNICATION DEVICES

By
Daniele Faccio
Laurea in Physics (Hons)

A thesis submitted for the degree of
Master of Philosophy

(Master Copy)

Department of Electronics and Computer Science,
University of Southampton,
United Kingdom.

May 2001

Certificate of Originality

I hereby declare that this submission is my own work and that, to the best of my knowledge and belief, it contains no material previously published or written by another person nor material which to a substantial extent has been accepted for the award of any other degree or diploma of a university or other institute of higher learning, except where due acknowledgement is made in the text.

I also declare that the intellectual content of this thesis is the product of my own work, even though I may have received assistance from others on style, presentation and language expression.

Daniele Faccio

UNIVERSITY OF SOUTHAMPTON

ABSTRACT

FACULTY OF ENGINEERING

ELECTRONICS AND COMPUTER SCIENCE DEPARTMENT

Master of Philosophy

A STUDY ON THE POSSIBILITY OF USING THERMALLY-POLED SILICA WAVEGUIDES FOR OPTICAL COMMUNICATION DEVICES

by Daniele Faccio

In the early 80's a series of experiments showed that it was possible to induce second harmonic generation in silica-glass fibres. The initial excitement was dampened when it was realised that the efficiency was very much limited only to be kindled once again by the first demonstration in 1991 of efficient second harmonic generation in bulk glass by thermal poling. Since then great progress has been made but many efforts are still being made to re-transfer this technology to fibre waveguides.

This thesis describes work done in order to assess the current state of art of thermal poling, the possibility of applying the technique to obtain efficient telecom devices and if there are any feasible solutions to the problems encountered in poling silica fibres.

The highest nonlinearity obtained in bulk silica glass by thermal poling is of the order of 1 pm/V and may be considered as the achievable limit in silica fibres. On this basis it can be shown that electro-optic modulation or switching in poled waveguides is not competitive with other more established technologies whereas all-fibre frequency conversion remains an interesting application.

It has, however, been noted that the induced nonlinearities in fibres are usually much smaller than in bulk glass. After an initial study of various charaterisation methods and a substantial refinement of the Makers Fringe Technique, we proceeded to model and experimentally determine the ionic migration process underlying thermal poling in silica. Further experiments showed that the presence of a germanium doped region hinders considerably the nonlinearity formation and some solutions were put forward. Most notably, we thermally poled for the first time microstructured holey fibres which are of great interest for nonlinear applications.

Acknowledgements

The work described in this thesis would have been impossible without the support and expertise passed onto me by my supervisors Peter and Valerio and especially by Gabs who taught me all the "tricks". I especially thank all those people with whom I worked and who never hesitated in passing on knowledge based on years of experience, H. Gnewuch, B. Grappe, C. Pannell, D.J. Richardson and T.M. Monro among others. I must also thank D.W.J. Harwood for the fibres with all the wanted (and unwanted) "features" and, in particular, for being so generous with his waveguide samples. I musn't forget my office-mates, Marco, Gilbo, Vic, Stavros, Alessandro and Huai Hoo who made life a lot easier (and sometimes a lot less easier).

I would finally like to briefly acknowledge my appreciation to Silvia for following me here from Italy without ever questioning my decisions and supporting me in many occasions.

Contents

Chapter 1

General Introduction

1.1 Fibre-based devices for WDM networks

WDM network telecommunications is currently undergoing a large scale transformation involving both the single users, with a demand for ever higher transmission capacity, and the actual network which is adapating to accommodate higher transmission rates and a larger bandwidth. Single mode fibres deployed in the telecommunications network can potentially accommodate more than 10 Tb/s traffic and WDM techniques offer a very efficient utilisation of the available bandwidth in the wavelength domain rather than in the time domain. The number of independent paths or addresses in a WDM network is given by the number of available wavelengths and, although this number may be large enough to provide the required transmission rates, problems may arise at interconnection nodes: for example, identical wavelength channels cannot be routed to the same output and must be converted to different wavelengths. Various schemes have been proposed for wavelength conversion which can be divided into three categories [1]:

1. optoelectronic wavelength converters: they involve electronic detection and successive retransmission
2. optical gating wavelength converters: these change their characteristics depending on the intensity of the input signal. A second continuous-wave probe signal monitors these changes and thus acquires the information carried by the input beam. Examples are devices based on semiconductor optical cross-gain or cross-phase modulation.
3. wave-mixing wavelength converters: it is these that we are most interested in. Nonlinear interactions between two input beams generate a third beam at a new wavelength. The wave mixing process can be induced by a material with a third-order nonlinearity (four wave mixing) or a second-order nonlinearity (three-wave mixing)

Four-wave mixing has already been exploited to this end however the low conversion efficiencies (in order to use the glass nonlinearity, silica-glass fibre lengths of the order of 1 km must be used) and the presence of a generated satellite signal make second-order nonlinearity based devices much more attractive. The main advantages of a three-wave-mixing wavelength converter (and, more in general, of all wave-mixing converters) are:

- complete transparency due to the all optical conversion mechanism
- the possibility to simultaneously convert many wavelengths in a three-wave mixing configuration which has no significant cross-mixing terms (as compared to a four-wave mixing process)
- there is no excess noise present in other converters which use amplifier stages
- the energy conservation relation $\omega_{\text{pump}} - \omega_{\text{input}} = \omega_{\text{output}}$ (where ω_{pump}, ω_{input} and ω_{output} are the pump, input signal and output signal frequencies respectively) implies that the chirp of the input signal is reversed during the wavelength conversion
- large bandwidths can be achieved

The main drawback is the fact that, in order to employ materials with a second-order nonlinearity ($\chi^{(2)}$), care has to be taken during the fabrication of the device that phase-matching (i.e. conservation of the total momentum) is achieved. Such phase-matched devices in a planar waveguide geometry have already been suggested ([2, 3]) but are afflicted by high losses due to both inefficient coupling from the fibre to the waveguide and also due to the actual material. In the future efficient all-fibre $\chi^{(2)}$-based wavelength converters would be desirable and a first demonstration of such a device is indeed the aim of this work.

The main obstacle encountered is, of course, that the amorphous silica glass structure is centro-symmetric and has no intrinsic $\chi^{(2)}$.

It was initially Osterberg et al. who discovered in 1986 that a second-order nonlinearity grating could be photo-induced in a silica fibre if a high power pump beam was launched into the fibre along with a much weaker second-harmonic (SH) seed. The grating nonlinearity had a value of $\sim 10^{-4} - 10^{-3}$ pm/V and the formation mechanism was finally explained on the basis of a new phenomenon: the photogalvanic effect [4]. Some years later Myers et al. ([5]) demonstrated that it was possible to induce a much higher $\chi^{(2)}$ (of the order of 1 pm/V) by thermal poling, i.e. by heating the glass and applying a large (kV) voltage. These discoveries have stimulated many areas of research and the use of the induced second-order nonlinearity (SON) has been proposed for a number of optical communication devices which mainly involve not only frequency conversion but also all optical or electro-optic switching. The use of such a low SON ($LiNbO_3$ has a $\chi^{(2)}$ more than an order of magnitude larger) is well accounted for by the high figure of merit available with

silica-glass fibres

$$\frac{|\chi^{(2)}|^2 \cdot (L \cdot B_w)^2 \cdot I}{\alpha \cdot n^3} \tag{1.1}$$

where L is the interaction length, I is the fundamental wavelength intensity, B_w the bandwidth of the second-order process and α the absorption coefficient. Overall it seems that the most promising application for poled glass will use the SON at optical frequencies for example as a wavelength converter for areas such as WDM re-routing and switching, frequency doubling in fibre lasers and correlated-photon sources for quantum cryptography. However other applications may be envisaged. The electro-optic coefficient may not be high enough for direct modulation in high bit-rate systems (see next section) but other interesting possibilities are fibre sensors based, for example, on poled Fabry-Perot cavities or even DFB lasers. An external electric field will couple with the electro-optic coefficient to produce a change in the cavity refractive index thus changing the transmission (or emission) spectrum. In this case only small electro-optic coefficients are necessary to detect even small electric-fields.

1.2 Evaluation of the necessary nonlinearity for some possible applications

1.2.1 Frequency conversion

In a difference frequency generation (DFG) process the frequencies are related by the energy-conservation relation, i.e. by $\omega_{\text{output}} = \omega_{pump} - \omega_{input}$. The conversion efficiency of such a process can be evaluated by taking measured values for SH generation: the SHG conversion efficiency is the same as that at degeneracy for DFG (i.e. for $\omega_{\text{input}} = \omega_{\text{output}}$ and, therefore, $\omega_{\text{output}} = \omega_{\text{pump}}/2$) and will not vary substantially off degeneracy. In a quasi-phase-matched configuration the SH generation conversion efficiency can be written as:

$$\begin{aligned} \eta &= \frac{P_{2\omega}}{P_\omega} = \frac{2\omega^2}{n_{2\omega} n_\omega^2 \epsilon_o c_o^3} \frac{P_\omega}{A_{\text{OVL}}} L^2 d_{\text{eff}}^2 \\ A_{\text{OVL}} &= \frac{1}{|\int\int f_\omega^2(x,y) f_{2\omega}^*(x,y) \mathrm{d}x\mathrm{d}y|} \\ d_{\text{eff}} &= \frac{A_{\text{OVL}}}{m\pi} \left| \int\int f_\omega^2(x,y) d(x,y) f_{2\omega}^*(x,y) \mathrm{d}x\mathrm{d}y \right| \end{aligned} \tag{1.2}$$

where ω is the fundamental frequency, P_ω and $P_{2\omega}$ are the fundamental and SH powers, respectively, $d(x,y)$ is the spatial distribution of the nonlinear coefficient (along the direction of propagation z the nonlinear coefficient is supposed to be $+/0$ modulated), d_{eff} is the effective nonlinear coefficient that depends on the m^{th} QPM

order and includes the overlap between poled region and the interacting modes, $f_\omega(x,y)$ is the transversal field distribution in the fibre, L is the grating length, $n_{2\omega}$ and n_ω are the refractive indices at 2ω and ω respectively and A_{OVL} is an equivalent area that depends on the overlap integral between the interacting fields.

In 1999 Pruneri et al. reported an average ~20% conversion efficiency of nanosecond pulses at 1532 nm with ~4 kW fundamental peak power [6]. This result was obtained in an NA=0.19 D-shaped fibre with a ~7 cm long thermally poled region and the nonlinearity, measured[1] as 0.05 pm/V, was +/0 modulated with a periodicity such that the SHG process was quasi-phase-matched. The conversion efficiency in $\%/W$ or dB units was $5 \cdot 10^{-3}\%/W$ or -43 dB (supposing a 1 W pump power). This figure isn't very impressive but in this work extensive measurements on different grade bulk silica glass show that $d = 0.5\ pm/V$ can be achieved. If such a nonlinearity were to be induced in the fibre core then the converted signal power ($\propto d^2$) would increase by a factor 100 and the conversion efficiency η increases to -23 dB. Increasing the fibre nonlinearity to 0.5 pm/V should be possible as this is the value typically found in bulk glass. Investigation of why the fibre nonlinearity is an order of magnitude lower is the object of chapter 4 and some possible solutions are proposed in the concluding chapter.

A further improvement can be obtained by solving a merely technological problem and creating longer quasi-phase-matching gratings. The output signal power scales as L^2 so a 20 cm long grating will increase η to -14 dB and 1 m will give $\eta \sim 0$ dB (see figure 1.1). Increasing the fibre length to $L = 20\ cm$ should not prove too difficult however, at longer lengths, different issues must be considered: writing an error-free 1 m long grating will be a challenging feat in itself and other complications, mainly related to the bandwidth of the conversion process and variations in the fibre geometry, may arise. The bandwidth for SHG is given by [7]

$$\Delta\lambda \simeq \frac{0.44\lambda^2}{c_o L \cdot GVM} \tag{1.3}$$

where λ is the fundamental wavelength and GVM is the group velocity mismatch defined by the relations

$$\begin{aligned} GVM &= |v_g^{-1}(2\omega) - v_g^{-1}(\omega)| \\ v_g(\omega) &= \left.\frac{\partial\omega}{\partial\beta}\right|_\omega \end{aligned} \tag{1.4}$$

[1] the d_{eff} coefficient was measured as 0.014 pm/V. For first-order quasi-phase-matching $m = 1$ and supposing a uniform distribution of the nonlinearity across the core region we have $d \simeq \pi d_{\text{eff}} \simeq 0.05$

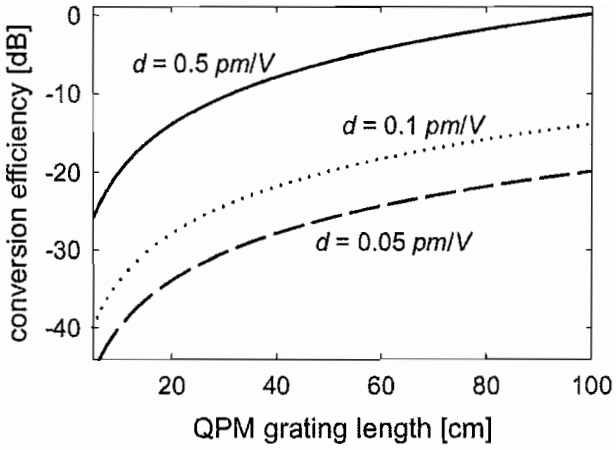

Figure 1.1: SH conversion efficiency as a function of the nonlinear quasi-phase-matching grating for 1 W pump power and three different second-order nonlinearity ($d = \chi^{(2)}/2$) values, 0.05, 0.1 and 0.5 pm/V as indicated in the figure. The calculations are semi-empirical: the dashed curve ($d = 0.05\ pm/V$) is based on measured conversion efficiencies [6] and the other two curves were obtained from the first by simply rescaling with the nonlinearity. The fluctuations in the fibre geometry have been ignored and the nonlinearity is assumed to have uniform distribution across the core region.

where $\beta = \beta(\omega)$ is the mode propagation constant in the fibre calculated using the characteristic equations [8]. With equations (1.3), (1.4) and (2.6) we can evaluate the GVM the bandwidth for conversion between LP_{01} modes at 1550 nm in a 10 cm long quasi-phase-matched grating to be $\sim$2 nm. It can be shown that a small variation, e.g. $1\%/m$, variation in the core radius along the length produces large changes in the peak phase-matched wavelength, $\sim$13 nm over 1 m of fibre. This means that after 15-20 cm the conversion efficiency will not grow anymore as the fundamental wavelength will not fall in the grating's bandwidth. The overall effect on a DFG process would be a lower conversion efficiency ($\sim -14\ dB$) but with a larger bandwidth for a process, for example, in which the input wavelength is fixed and a variable converted output wavelength is desired.
Overall, these figures are very promising and show that efficient all-fibre frequency converters are a feasible goal even if the nonlinearity is very low compared with other second-order materials.

1.2.2 Electro-optic modulation

Pockels-effect based devices use a SON described by $\chi^{(2)}(\omega_3 = \omega_1; \omega_1, 0)$ or, more frequently, by the r-coefficient ($r = 2\chi^{(2)}/n^4$ where n is the material refractive index [9]). For these devices other limiting factors, different from those for wavelength converters, must be considered. Let us consider, for example, an electro-optic modulator: in this case the bandwidth will be severely restricted by the length of the modulating electrodes. In $LiNbO_3$ modulators the bandwidth is limited to $\simeq$ 2 $GHz \cdot cm$ in a "lumped" electrode configuration and to $\simeq$ 10 $GHz \cdot cm$ in a

"traveling-wave" configuration [10]. These figures give a very rough estimate of the limitations also in glass and they indicate that silica glass based electro-optic modulators (with r in the 0.1-1 pm/V range) will only be able to cope with modulation bandwidths less than 1 GHz due to the long fibre lengths necessary to compensate for the low SON. It is worth noting that the low SON may also be compensated for by using a higher switching voltage: for example, a 36 cm long silica waveguide modulator with a 1700 V switching voltage has been demonstrated [11]. However,

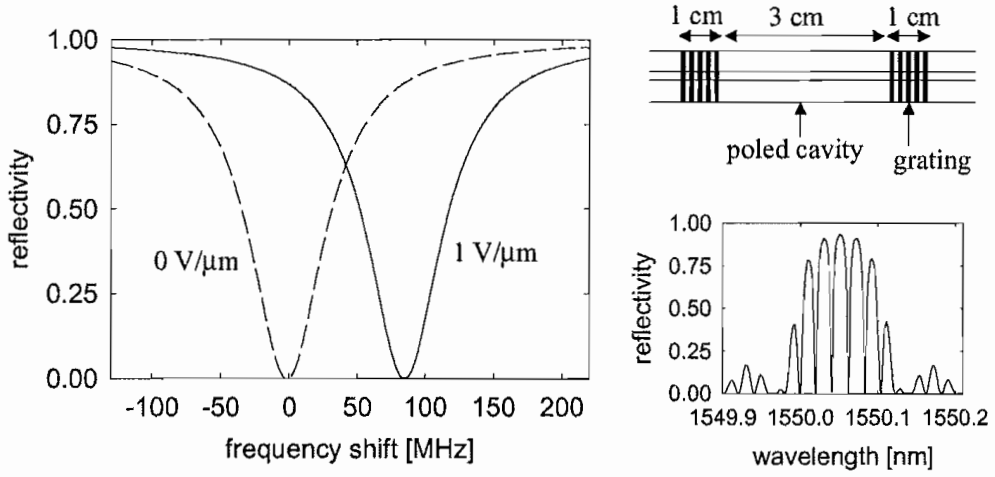

Figure 1.2: Frequency shift in the fibre-Fabry-Perot interferometer reflectivity when a 1 $V/\mu m$ external electric field is applied. Also shown are the overall reflectivity spectrum (bottom right) and the cavity design (top right) used for these calculations. The fibre NA is 0.32 and the two identical gratings are produced by a periodic refractive index increase of $2 \cdot 10^{-4}$.

restrictions on consumption costs require devices that use a voltage in the 1-10 V range and this may lead to prefer more established materials (e.g. $LiNbO_3$ or AlGaAs) that work with such powers. A low electro-optic coefficient is, indeed, a limitation for modulators in telecom systems but may still prove useful in other devices such as electric-field sensors where the electric field to be measured induces a phase shift in the poled arm of a fibre interferometer. The sensitivity of such a device may be greatly enhanced by using a poled Fabry-Perot interferometer or DFB laser. The reflectivity of a Fabry-Perot cavity made by two Bragg gratings enclosing a poled region can be calculated using multiplying the matrices associated with the various cavity elements [12]. Supposing that the cavity is made in an $NA = 0.32$ fibre by two 1 cm long grating mirrors 3 cm apart, that the photoinduced refractive index change is $\Delta n = 2 \cdot 10^{-4}$ and the Bragg wavelength (at which the reflectivity is maximum) is 1.55 μm and that the thermally poled cavity region has an electro-optic coefficient of 0.5 pm/V then an electric-field of 1 $V/\mu m$ induces a $\sim$100 MHz shift in the transmission peak at the Bragg wavelength (see figure 1.2). The same external electric field will also induce a $\sim \pi/35$ phase shift in

the reflected wavelength: such phase (or frequency) shifts can be measured using interferometric techniques and thus prove the feasibility of basing such devices on thermally poled fibres.

1.3 A general overview of this thesis

Still little is known about the poling process and the distribution of the nonlinearity. Although many measurements have been made in the hope of optimising the nonlinearity and understanding the formation mechanism. Various poling techniques and glasses have been tested often obtaining contrasting results. Table 1.2 shows a summary of the most recent and significant results. Our group has concentrated mainly on silica glass which seems, at the moment, the most promising in view of both the obtainable nonlinearities and future exploitation in actual devices. In 1998 a 1.2% SH conversion efficiency from a poled fibre using 100 fs pulses from a Ti:sapphire laser was reported [13]. A year later, greater than 20%-efficient SH generation was observed using nanosecond pulses (4.5 kW peak-power) at 1530 nm [6]. These results opened the way to the experiments carried out by Bonfrate et al. demonstrating the possibility to generate parametric fluorescence and correlated photon pairs [14]. However, these and other measurements (see [15] and Table 1.2) also pointed out some limitations in the maximum nonlinearities and conversion efficiencies that can be obtained in silica fibres. It was apparent that only in certain (and rather elusive) conditions it was possible to generate a SON in fibres that had the same order of magnitude of that found in bulk silica glass. In most cases the nonlinearity at 1.5 μm was 5 to 10 times smaller than in bulk silica and strong evidence of a non-symmetric arrangement of the nonlinearity around the fibre core was observed (a deeper analysis of the problem will be given in chapter 4). A factor 10 decrease in the expected SON will give rise to a decrease by a factor 10^2 in the SH conversion efficiency and it was therefore necessary to look deeper into the poling process and explain our results. In chapter 2 we describe a new thin-film characterization technique which we then used to study the evolution of the nonlinear thickness and coefficient in poled glass samples (chapter 3). These measurements highlight a strong dependence on sample thickness and can be used in future to tailor the nonlinear layer to different waveguide geometries. The results, along with

glass	OH	Na	K	Al	Li	$\rho\ (\Omega \cdot cm)$	n_{1064}
Herasil 1	≈ 150	1	0.8	20	1	$\sim 10^{10}$	~ 1.45
Suprasil 1	$\leqslant 1000$	0.05	0.01	0.05	0.01	$\sim 10^{10}$	~ 1.45
Suprasil 300	< 1	0.05	0.01	0.05	0.01	$\sim 10^{10}$	~ 1.45

Table 1.1: Impurity contents in ppm (μg/g), resistivity at $300°C$ and refractive index at 1064 nm for three different commercial glasses from Heraeus. Suprasil 300 is similar to the synthetic silica used in fibres.

those published by others, enable us to tentatively model the ion-migration mechanism responsible for the nonlinearity formation. The model presented in chapter 3 cannot explain every aspect of thermal poling but it does touch some of the more fundamental aspects of the process, giving a better overall understanding of the role played by impurity concentrations and poling conditions. The knowledge thus acquired was enough to start speculating on which parameters may be varied in the hope to optimise the nonlinearity. Na-injection and UV-enhancement are two fruitful ideas, described in chapter 5: whereas the former induces a rather non-uniform and unstable nonlinearity, the latter enables efficient poling of Suprasil grade silica and offers a new possibility for creating nonlinear gratings. Finally, chapter 4 describes the our work on poled optical waveguides. We have proved that, as we already suspected, the nonlinearity does not penetrate the germanium doped core region and a solution to this problem has been proposed. Furthermore we report the first demonstration of thermal poling in microstructured fibres (also known as photonic crystal or holey fibres).

Different silicate glasses have been investigated in this work. Table 1.1 lists the main impurity contents, resistivity at $300°C$ and refractive index at 1064 nm for the three most important glasses used: Herasil 1 and Suprasil 1 from Heraeus and Suprasil 300 (also from Heraeus) which is very similar to the synthetic silica used in fibres. Table 1.2 lists some of the most important results and measurements obtained for various poling techniques and glasses.

glass	fibre	bulk	$\chi^{(2)}$ (pm/V)	$\chi^{(3)}$ $(10^{-22}m^2/V)$	L (μm)	ref
silica cover slips		✓	1		4	[5]
"wet" Suprasil		✓	0.6		< 3	[16]
"wet" Suprasil		✓	0.4			[17]
Silica		✓	1.4		10	[18]
Sol-gel silica		✓	1.07		20	[19]
Herasil		✓	0.93	1.8		[20]
Herasil 1		✓	0.68		8	[21]
Herasil		✓	0.1		4.5	[22]
Herasil 1		✓	0.41		36	[19]
Herasil 1		✓	1	4	4	[23]
$ZnO:TeO_2$		✓	0.44		1000	[24]
$MgO:ZnO:TeO_2$		✓	0.26		1000	[24]
$KO_2:Cs_2O:TiO_2:SiO_2$		✓	0.017			[25]
$NO_3:TeO_2$		✓	9 $^{\perp}$		15 $^{\perp}$	[26]
ZF_7		✓	4		4	[27]
Ge:SiON-film §		✓	0.09		2	[28]
Ge:SiON-film		✓	22±8		2	[29]
GeO_2-film $^{\natural}$		✓	25		1	[30]
GeO_2-SiO_2 §	✓			3.8		[31]
GeO_2-SiO_2 §	✓		0.7			[32]
$GeO_2:SiO_2$ §	✓		0.8			[33]
$GeO_2:SiO_2$ $^{\natural}$		✓	6.8		4	[34]
GeO_2-SiO_2 ‡		✓	0.66		1	[35]
GeO_2-SiO_2 $^{\parallel}$	✓		0.2		1	[36]
GeO_2-SiO_2	✓		0.014 $^{\flat}$			[6]
GeO_2-SiO_2 §	✓		0.015			[37]
GeO_2-SiO_2	✓		0.2			[38]
GeO_2-SiO_2 §	✓		0.05			[39]
GeO_2-SiO_2	✓		1.4			[40]

Table 1.2: Summary of the most relevant published results for poling. $\ddagger$ = e-beam poling, $\natural$ = UV-poling, $\parallel$ = CO_2-poling, § = electro-optic measurements, $\perp$ = estimated, $\flat$ = d_{eff} (d/π)

Chapter 2

Two-Beam Noncollinear Makers Fringe Technique

2.1 Introduction

It is now firmly established that during thermal poling a thin depletion region is formed under the anodic surface and it is in this region that the second order nonlinearity is concentrated. Many experiments also indicate that the $\chi^{(2)}$ is established via the intrinsic $\chi^{(3)}$ and the frozen-in static electric field E_o:

$$\chi^{(2)}(\omega_3 = \omega_1+\omega_2;\omega_1,\omega_2) = 3\chi^{(3)}(\omega_3 = \omega_1+\omega_2;\omega_1,\omega_2,0)E_o = 3\chi^{(3)}\frac{V}{L} \qquad (2.1)$$

One of the most relevant quantities in understanding the poling process is the nonlinear depth L. This can be measured in different ways but the most used is the Makers Fringe Technique (MFT) extensively described in [41]. The technique is experimentally straight-forward: a fundamental beam with frequency ω is focused onto the sample and the second harmonic (SH) power is recorded whilst the nonlinear thickness is varied, e.g. by rotation of the sample. From spacing and position of the SH peaks one can infer L whereas $d_{\text{eff}} = \chi^{(2)}/2$ ([42]) can be estimated by comparison with a reference sample of known nonlinearity [41]. However, acceptable resolution for L is possible only when L is greater than the coherence length (ℓ_c), i.e. the distance over which the SH field and the SH polarisation wave (proportional to the square of the fundamental field) become π out of phase:

$$\ell_{\text{c}} = \frac{\pi}{\left|\Delta\vec{k}\right|} = \frac{\pi}{\left|\vec{k}_{2\omega} - \vec{k}_{\omega,1} - \vec{k}_{\omega,2}\right|} \qquad (2.2)$$

where $\vec{k}_{2\omega}$ and $\vec{k}_{\omega,1}$, $\vec{k}_{\omega,2}$ are the SH and the two fundamental wave-vectors, respectively. Indeed, in the one-beam MFT the smallest measurable value for L is

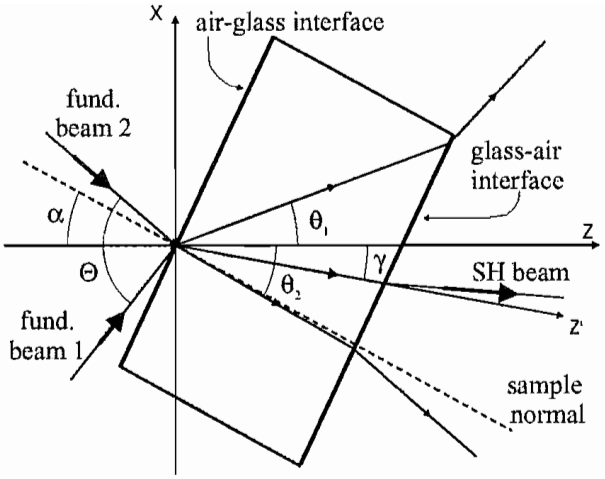

Figure 2.1: Geometrical layout of the noncollinear Maker Fringe technique: the plane $\hat{x}\hat{z}$ is defined as the lab reference system (taken so that $\hat{z}$ is the symmetry axis of the two incident beams). θ_1, θ_2 and γ are the two fundamental beam and second harmonic internal propagation angles. α is the sample tilt angle and Θ the relative angle between the two input fundamental beams.

determined by the largest internal angle attainable in the sample, corresponding to total internal reflection for the SH at the back material-air interface. In silica glass, at 532 nm SH wavelength, this angle is 43.6^o and indicates that a nonlinear region induced by thermal-poling can be fully characterised only if $L > \ell_c \cos(43.6) \simeq 18$ μm ($\ell_c = 24$ μm), which often is not the case [43].

A technique proposed by Pureur et al. overcomes this limitation by placing the sample between two glass prisms and thus eliminating the total internal reflection, making it possible to reach larger internal angles and correspondingly resolving smaller L [21]. A further improved scheme, based on the same principle and using hemispherical lenses, has also been proposed [44]. In this chapter I shall describe a new technique that can measure small nonlinear depths (< 2 μm) with high resolution (< 0.5 μm). Although we will refer our examples to silica, the contents of this chapter can be applied to any dispersive nonlinear thin film. Fig 2.1 is a schematic layout of the experimental geometry. Two identical fundamental beams, with field amplitudes $E_{\omega,1}$ and $E_{\omega,2}$ and with a relative external angle (Θ), overlap in the sample thus generating a polarisation wave at 2ω, $P_{2\omega} \propto \mathrm{d_{eff}}(E^2_{\omega,1} + E^2_{\omega,2} + 2E_{\omega,1}E_{\omega,2})$. The first two terms, with wave-vectors $2\vec{k}_{\omega,1}$ and $2\vec{k}_{\omega,2}$ respectively, will generate the so-called collinear-SH fields whereas the third term, with wave-vector $\vec{k}_{\omega,1} + \vec{k}_{\omega,2}$, will generate a noncollinear-SH field. It is worth observing that rigorously the SH fields (free waves) have slightly different propagation directions from those of the corresponding SH polarisations (bound waves).

Similarly to the one-beam MFT, variation of the sample inclination angle (α) will change the nonlinear depth traversed by the incoming fundamental beams. The

noncollinear-SH power will oscillate periodically, reaching a maximum value at distances that are odd multiples of ℓ_c. The output second harmonic power is given by

$$W_{2\omega} \propto \int_{-\infty}^{\infty}\int_{-\infty}^{\infty} | \int_0^L E_1^{\omega} E_2^{\omega} e^{i\cdot\Delta k\cdot z} d_{\text{eff}}(z) dz|^2 dxdy \tag{2.3}$$

so it can be seen that if L is varied continuously by rotating the sample then $P^{2\omega}$ is an oscillating function of the rotation angle α. The number of zeros observed is determined by Δk or, equivalently, by ℓ_c which in turn depends on the material, on the wavelengths and on the interaction geometry involved. As is shown in the next section, if instead of one beam we use two beams separated by an angle Θ and measure the noncollinearly generated SH, then the polarization wave and the second-harmonic wave have a much larger phase mismatch and thus the process involves a much smaller coherence length. In the same case as above, but with two fundamental beams at $\Theta = 90^o$, we find $\ell_c \sim 1\mu m$ (the resolution of our technique).

2.2 Equations

We must rewrite equation (2.3) using the correct expressions for the input fields, Δk and d_{eff}. The beams used for the experiments always had diameter significantly larger than the nonlinear film thickness under measurement, so the electric fields (both incident and generated) may be taken in a first approximation as plane waves. In the two-beam case, the projection of $\vec{\Delta k}$ along the SH field internal propagation direction (z') is given by

$$\Delta k'(\Theta,\alpha) = \frac{4\pi}{\lambda}\left\{ n\left(\frac{\lambda}{2}\right) - \frac{n(\lambda)}{2}\left[\cos\left(\theta_1(\Theta,\alpha) - \gamma(\Theta,\alpha)\right) + \cos\left(\theta_2(\Theta,\alpha) - \gamma(\Theta,\alpha)\right)\right]\right\} \tag{2.4}$$

where λ is the fundamental wavelength, $\theta_1(\Theta,\alpha)$, $\theta_2(\Theta,\alpha)$ and $\gamma(\Theta,\alpha)$ are the two fundamental fields and SH field internal propagation angle, respectively (as shown in fig 2.1). They are defined in the laboratory reference system, taken so that $\hat{z}$ is the symmetry axis of the two incident beams, by:
$\theta_1(\Theta,\alpha)$=$\sin^{-1}\{[\sin(\Theta/2+\alpha)]/n_\omega\} - \alpha$,
$\theta_2(\Theta,\alpha)$=$\sin^{-1}\{[\sin(\Theta/2-\alpha)]/n_\omega\} + \alpha$ and
$\gamma(\Theta,\alpha)$=$\sin^{-1}\{n_\omega/n_{2\omega}\sin[(\cos\theta_1 + \cos\theta_2)/2]\}$.
This last expression is obtained from the boundary conditions for SH generation at the interface between a linear and a nonlinear medium, i.e. from the continuity of the magnetic and electric field tangential components [45].

As can be seen in equation (2.3), integration is also carried out along x and y in order to include finite volume effects which may change the amplitude of the SH power oscillation. However it is worth noting that this effect can be completely ignored in the y direction: integration in this direction results simply in a constant multiplication factor given by $\int exp(-y^2)$. Therefore, using equation (2.3), the overall normalised SH conversion efficiency ($\eta_{\mathrm{SH}} = W_{2\omega}/W_{\omega}^2$), dependent on both α and Θ, can be written as

$$\eta_{\mathrm{SH}}(\Theta,\alpha) = \frac{2\omega^2}{\varepsilon_o c_o^3 n_\omega^2 n_{2\omega}} \frac{u(\Theta,\alpha)}{\pi \mathrm{w}_o^2} T_{2\omega} T_{\omega,1} T_{\omega,2} \cdot \cdot \int_{-\infty}^{\infty} dx \left| \int_0^{\frac{L}{\cos\gamma(\Theta,\alpha)}} \mathrm{d}_{\mathrm{eff}}(\Theta,\alpha,z') e^{i\Delta k'(\Theta,\alpha)z'} dz' \right|^2 \quad (2.5)$$

where P_ω and $P_{2\omega}$ are the incident fundamental and output SH powers measured after the sample, w_o is their beam waist ($1/\mathrm{e}^2$ intensity radius), n_ω the material refractive index at ω and $n_{2\omega}$ at 2ω, ε_o is the vacuum dielectric permittivity and c_o the velocity of light in vacuum. $T_{\omega,1}$, $T_{\omega,2}$ and $T_{2\omega}$ depend on Θ and α and are the fundamental and SH power Fresnel transmissivities, respectively. $u(\Theta,\alpha)$ is a projection factor for the beam area which takes account of beam expansion due to refraction at the sample interface. Finally, $\mathrm{d}_{\mathrm{eff}}(\Theta,\alpha,z')$ is the projection of the excited $\mathrm{d}_{\mathrm{eff}}$-tensor components along the direction normal to z' with a spatial profile described by the z' dependence. The complete expressions used for the actual calculations can be found in appendix A.

2.3 Results

As already discussed, the smallest nonlinear depth that can be measured using the Makers fringe technique is determined by the coherence length. Figure 2.2 shows ℓ_c as a function of the external angle between the two incident pump beams. As a comparison, ℓ_c has been plotted for two materials: SiO_2 and $LiNbO_3$ (z-cut). The higher $LiNbO_3$ dispersion allows a better resolution at $\theta = 0$, i.e. in the one-beam configuration. However, at larger angles, the resolution obtainable in the two materials becomes equivalent.If λ is the fundamental wavelength then for $\theta \sim 0^o$ we have $\Delta k \sim \frac{2\pi}{\lambda}(n_{2\omega} - n_\omega)$ and there is a strong material-dispersion dependence but, for $\theta \to 180^o$, $\Delta k = \frac{4\pi}{\lambda} n_{2\omega}$ and ℓ_c will be similar ($\sim 1\ \mu$m) for most materials. The Sellmeier equations used for SiO_2 are:

$$n(\lambda) = \sqrt{1 + \frac{0.6813\lambda^2}{\lambda^2 - 0.0045} + \frac{0.4231\lambda^2}{\lambda^2 - 0.0135} + \frac{0.8713\lambda^2}{\lambda^2 - 95.55}} \quad (2.6)$$

and for $LiNbO_3$ (z-cut) [46]:

$$no(\lambda) = \sqrt{4.913 + \frac{0.118717}{\lambda^2 - 0.045932} - 0.0278\lambda^2} \tag{2.7}$$

In the case of SiO_2 thermally poled in air, the nonlinear region usually varies in the

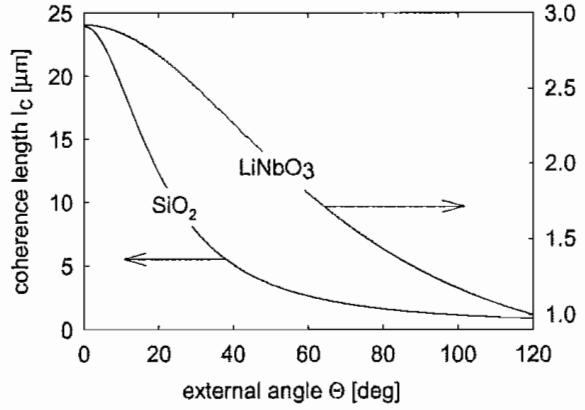

Figure 2.2: The coherence length ℓ_c, for a noncollinear SH generation process, against the external angle θ between the two incident pump beams for SiO_2 and $LiNbO_3$.

range 4-16 μm [43]. Therefore we chose $\theta = 90^o$ which is easy to arrange experimentally and guarantees a high resolution. Indeed, taking the value of ℓ_c from figure 2.2, nonlinear depths as small as $\ell_c \cos(43.6) \simeq 1.5\mu$m can be measured. Figures 2.3 a) and b) show the calculated second harmonic angular dependence for three nonlinear depths (5 μm, 9 μm, 14 μm) in the one beam and two beam configuration respectively. It is obvious that the two beam configuration provides an extremely high (sub-μm) resolution for depths smaller than 15 μm, where the one-beam technique completely fails. There is also an intrinsic degeneracy in the one-beam MFT due to the fact that nonlinear depths which are integer multiples of the coherence length give normalized second harmonic powers which can be impossible to distinguish experimentally. In other words, a certain normalized SH distribution may be given by a nonlinear depth L but may be experimentally indistinguishable from that given by a depth $L + n\ell_c$ (where n is an integer). Any such cases of "degeneracy" may now be removed by repeating the measurement for a different θ and comparing the measurements.

The experimental layout used for the measurement of the noncollinear Maker fringes is shown in figure 2.5. The laser used was a Q-switched and actively-modelocked Nd:YaG laser of 1064 nm fundamental wavelength with an average power of 3 W and a 300 ps pulse duration. A half wave plate controls the polarisation of the fundamental pulses before they are split by a 50% beam-splitter and focused onto the sample. The SH signal was measured with a photo-multiplier tube after eliminating

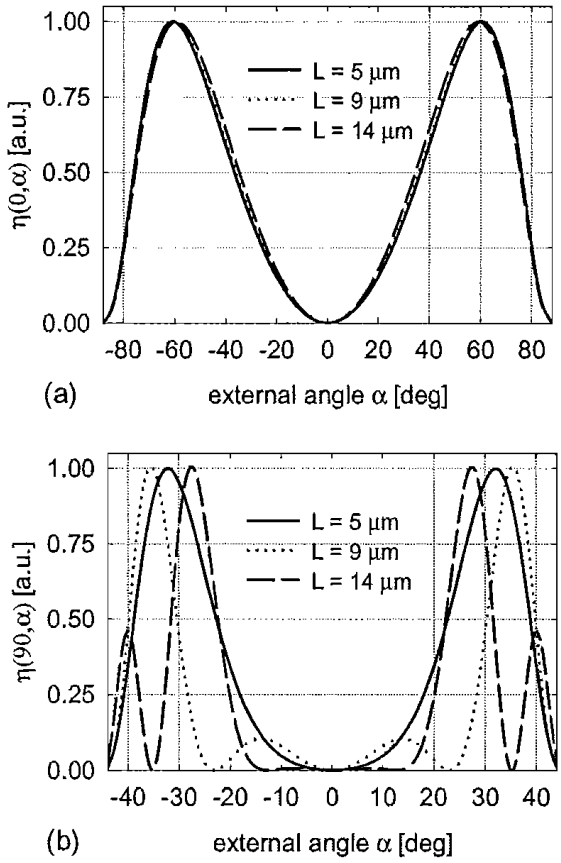

Figure 2.3: calculated second harmonic angular dependence for three nonlinear depths (5 μm, 9 μm, 14 μm) in the one beam (a) and two-beam (b) configuration.

the fundamental beam using an interferometric filter. Once L is known the nonlinear coefficient is found by normalising the collinear SH with respect to that from a reference quartz sample. Figures 2.4 a) and b) show the second harmonic signal as a function of the sample angle obtained using the noncollinear makers fringes technique. The samples (Herasil silica from Heraeus) were thermally poled at 280^o, 4 kV for 10 and 30 minutes respectively. The accuracy of the NCMFT measurements were then controlled using a standard HF-etching measurement. The curves are easily distinguishable even if L is well below the 18 μm limit for the one-beam MFT and the difference between the two L values is smaller than 1 μm. The solid lines are the best fits obtained using eq. 2.5 and a truncated gaussian profile for d_{eff} (see figure 2.6).

It is worth noting that there is a trade-off between the maximum pump-beam angle used to increase the resolution and the actual resolution obtained. This is due to the fact that at large pump-beam angles the maximum sample-tilt angle becomes increasingly smaller. Furthermore the second-harmonic conversion efficiency decreases with decreasing coherence length i.e. with increasing pump-beam angle.

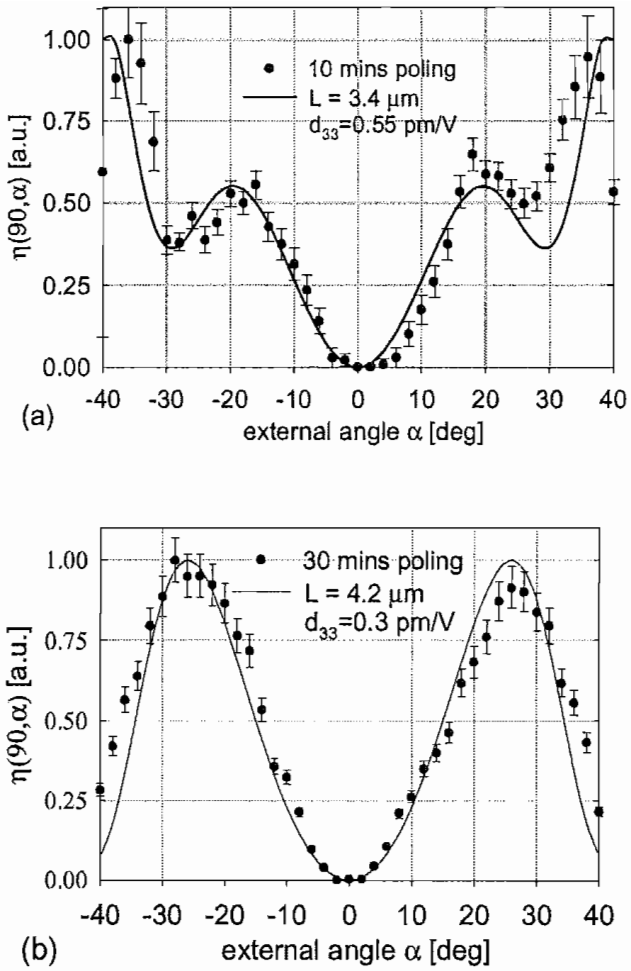

Figure 2.4: A sample poled for 10 minutes at 280^oC and 4 kV, shows a nonlinear depth of 3.4 μm (a) another, poled under the same conditions for 30 minutes, shows a nonlinear depth of 4.2 μm

A 90^o angle between the two pump beams is experimentally very easy to control and, with a maximum sample-tilt angle of 45^o and a measurable SH, gives the best results for our poled silica samples.

In conclusion, the new technique described in this chapter gives the possibility to completely characterise thin nonlinear films, i.e. measure both nonlinear thickness and coefficient. This technique is preferable to others for many reasons:

- it can resolve nonlinear thicknesses as small as 1 μm with sub-micron resolution
- it is non-destructive (HF-etching is usually used in measuring nonlinear thicknesses smaller than the material coherence length)
- the experimental set-up is an easy-to-implement modification of the standard one-beam Makers Fringe Technique

The only true drawback to this technique is the reduced second-harmonic generation efficiency in a noncollinear configuration with respect to the standard collinear

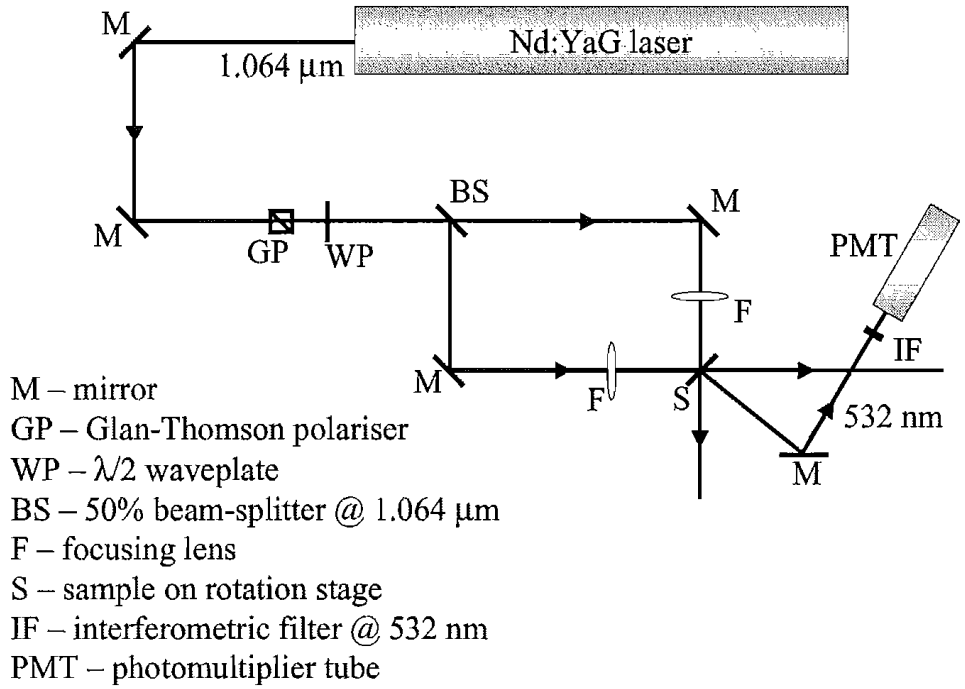

Figure 2.5: Experimental layout for the noncollinear Maker Fringe measurements.

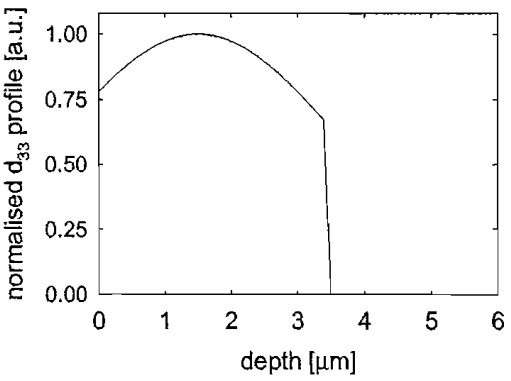

Figure 2.6: Example of truncated gaussian profile, found to be the best when fitting experimental data with equation 2.5. The nonlinearity profile shown was used to fit the data in figure 2.4 a).

technique. If the nonlinear coefficient to be measured is small (less than 0.1 pm/V) and a large angle between the two beams is used ($\geqslant 60^o$) then the generated second harmonic may be so small that a photon counting system is required to measure the power. Furthermore, it is worth noting that when the coherence length is significantly reduced ($\sim 1\ \mu m$), for example by using a 90^o angle between the two beams, then the Maker's fringes in the second harmonic power can become rather noisy. This is most probably due to the fact that the micron-sized irregularities in the nonlinear layer are no longer averaged out in the nonlinear process. The dimension of these irregularities seems to increase with the nonlinear depth in poled

glasses. We found that for nonlinear depths between 1 and 5 μm the optimum angle between the two beams is 90°. For thicker nonlinearities a smaller angle between the two pump beams should be used, thus increasing the coherence length and reducing the noise from any irregularities.

Chapter 3

Second order nonlinearity formation dynamics in thermally-poled silica-glass: modeling and measurements

3.1 Introduction

Before proceeding to discuss experimental results obtained using the noncollinear Makers fringe technique (described in chapter 2) and other experiments which are still underway, it is best to examine more closely the mechanism responsible for thermal poling in silica glass.

The issue is fairly complex. Two processes, which can explain thermal poling, have been proposed: re-orientation of dipoles (namely dipolar defects) and ionic-migration. The former has a well defined theory ([47, 48, 49]) and has been extensively applied to orientationally ordered organic materials possessing second order nonlinearity. The latter is of major importance in many fields, ranging from electric-field assisted ion-diffusion for waveguides ([50, 51]) to MOS capacitor structures ([52]). However, a comprehensive theory which can explain all aspects of ionic glass conduction is still to be found [53, 54].

A commonly used technique ([5, 55]) to decide which of these mechanisms is dominant is the measurement of the ratio of the two non-zero components of the second-order nonlinear susceptibility tensor d_{33}/d_{31} (see eq (A.7)). If a space-charge field, induced by ionic migration, is the cause of the nonlinearity then d_{ij} is proportional to the third order nonlinear tensor (eq (2.1) with $d = \chi^{(2)}/2$ [42]) and, in a transparent isotropic medium, $d_{33}/d_{31} = 3$ [48]. On the other hand, if the mechanism is one of dipole orientation, then $d_{33}/d_{31} = 3$ in a weak orienting electric field and will depend on the ratio of hyperpolarizability components in a high field. Therefore,

it is possible to rule out a space charge electric-field mechanism if this ratio is not 3. A ratio of exactly 3 will provide support for an electric-field induced mechanism while not excluding the possibility of dipole orientation. Various values for d_{33}/d_{31} have been reported ranging from 2 to 7 [5, 55, 20]. It is worth noting, at this point, that these results would be rigorously conclusive only if the nonlinearity had a true isotropic-$C_{\infty v}$ symmetry. Indeed, an anisotropy of only a few percent would be able to account for such d_{33}/d_{31} values [56]. There are, of course, other arguments which have apparently settled the controversy: a dipole-orientation mechanism would necessarily take place in the whole bulk of the poled sample and would lead to a negative surface charge distribution at the anode (positive at the cathode). It is, however, well known that the nonlinearity has a thickness typically in the 2-30 μm range and shows a positive charge layer towards the anode [43]. Furthermore there is strong experimental evidence that ionic migration does indeed take place during thermal poling with a subsequent charge pile-up occuring at depths in good agreement with nonlinearity thickness measurements [57]. This experimental evidence has lead to the general belief that thermal poling can be explained by a space-charge induced electric-field mechanism.

In the first part of this chapter we describe a two-charge ion-migration model with which it is possible to calculate the evolution of the nonlinear thickness and of the internal electric field induced during thermal poling in silica glass. This model is similar in its results to that developed by Alley et al. [58] but uses rather simpler equations. The second part of the chapter is dedicated to the experimental characterisation of the nonlinearity formation dynamics is silica glass.

3.2 Modeling

3.2.1 Equations

During thermal poling, the silica-glass sample is heated typically to 280^oC and a positive 4-5 kV voltage is applied. The full equations which describe the induced ionic migration, considering both drift and diffusion, can be rather complicated and have been solved under simplified conditions (e.g. [58]). Our model is an extension of Von-Hippels original work [59] which considered only one ion species drifting. In this case the drifting ion species will be sodium (Na^+), the main charge carrier in silica-glass [60]. As the mobilised ions drift towards the cathode, two distinct regions form in the glass: a depleted region of negative space-charge (depletion region) followed by an un-depleted, neutral region. The depletion region forms under the anode with a monotonically increasing depth until the equilibrium value $L_\infty = \sqrt{2\varepsilon V/\rho}$ is reached, where ε is the glass dielectric constant, V the applied voltage and ρ the charge density in the depleted region. d_{33} also increases with t until the maximum value is reached at equilibrium (see figure 3.1). However, this

one-charge carrier model cannot account for many experimental results such as the multiple time scales during SH signal formation observed by Alley et al. [58], the non-monotonic time-evolution of d_{33} reported in this thesis (see fig. 3.5) and the continuous growth of the nonlinear depth even for very long poling times [43]
The next most mobile charge carrier in silica glass is H^+ ([60]) with a mobility (μ_H) which has been found to lie in the range 10^{-4}-10^{-3} μ_{Na} (μ_{Na} is the sodium mobility) [61, 62]. It has been demonstrated that, unless particular care is taken, the glass surface always has a high concentration of H^+ (or H_3O^+) at the surface [60]. Furthermore, if press-contact or non-blocking evaporated electrodes are used then hydrogen also continuously diffuses under the influence of the externally applied electric field from the external atmosphere into the glass [60, 61, 63]. Due to the fact that $\mu_H \ll \mu_{Na}$ three regions will form: straight under the anode a region with Na substituted by H (region I) - the charge in this region will depend on the amount of in-diffused H^+. This is followed by a negatively charged depletion layer (region II) and finally by the un-depleted neutral region (region III) (see figure 3.2). Von-Hippel's calculations can be retraced, posing the continuity of both current and electric field through the interfaces between regions I-II and II-III, thus obtaining two coupled differential equations

$$\begin{cases} \dfrac{dL_{Na}}{dt} = -\dfrac{\rho_{Na}}{\rho}\mu_{Na}\left(\dfrac{\rho}{\varepsilon}L_{Na} + \dfrac{\rho_H}{\varepsilon}L_H + A_t\right) \\ \dfrac{dL_H}{dt} = \mu_{Na}\left(\dfrac{\rho_H + \rho}{\varepsilon}L_H + A_t\right) \\ A_t = \dfrac{1}{S}\left(\dfrac{\rho}{2\varepsilon}L_{Na}^2 + \dfrac{\rho_H}{2\varepsilon}L_H^2 - \dfrac{\rho}{\varepsilon}SL_{Na} - \dfrac{\rho_H}{\varepsilon}SL_H - V\right) \end{cases} \tag{3.1}$$

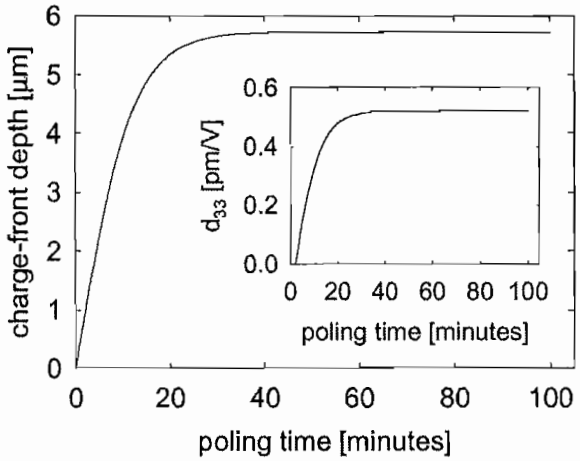

Figure 3.1: Calculated charge-front evolution using Von-Hippels one-charge model. In the inset is also shown the evolution of the d_{33}-coefficient. All parameters are the same as those used in figures 3.3 and 3.4.

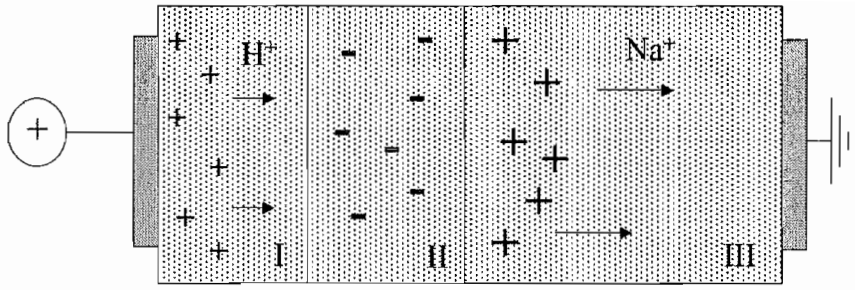

Figure 3.2: Glass thermal poling: the electric field created between the two electrodes induces ion-migration and, in a two-charge model, the formation of three regions - I (neutral with H^+ substituting for Na^+), II (Na^+-depleted and therefore negatively charged) and III (neutral).

where L_{Na} and L_H are the time dependent "charge-fronts" of the Na and H species, μ_{Na} and μ_H are their mobilities, ρ_{Na} and ρ_H the charge densities (> 0) and $\rho = -\rho_{Na}$ is the charge density of the negatively charged depletion region nd S is the the sample thickness. Diffusion blurring the boundaries has been neglected. The last equation in (3.1) is given by the boundary condition

$$-V = \int_0^{L_H} E_I dx + \int_{L_H}^{L_{Na}} E_{II} dx + \int_{L_{Na}}^{S} E_{III} dx \tag{3.2}$$

where E_I, E_{II} and E_{III} are the internal electric fields in the three regions I, II and III.

Cooling the sample after thermal poling will leave a frozen-in charge distribution with a consequent electric-field which, once the external electrodes have been removed, will attract charged particles from the surrounding atmosphere and will remain confined inside the glass. The electric field under the anode reaches values which are very close to the dielectric breakdown value of silica-glass, i.e. $\simeq 10MV/cm$ [64]. In fact, the maximum obtainable d_{33} may be limited by breakdown through an electronic current induced near the anode by the very high electric field [55, 60] and this would also explain the positive charge layer observed under the sample-anode surface [43]. In fact it is worth noting that the described model is based on the assumption that Na^+ and H^+ are the only charge carriers. This may well be the case in ordinary glasses, however the Na^+-depleted region is very different from the un-poled glass. The most mobile ions have been removed and an electric field close to the dielectric breakdown value is applied: under these conditions a non-ohmic electronic current is to be expected. However, such a process is very difficult to describe with mathematical equations and the as-described model (i.e. using only two positive ionic species) still remains an important step forward from the one-ion model towards a deeper understanding of thermal poling.

3.2.2 *Results*

The equations were solved using a fourth order Runge-Kutta method. ρ_{Na} was derived from the concentration (1 ppm) of Na in Herasil 1 glass and we made the assumption that H^+ completely substitutes for Na^+, i.e. $\rho_H = \rho_{Na}$ [60]. Reported values for the Na^+ mobility (μ_{Na}) in silica-glass vary greatly depending mainly on impurity concentrations: for 1 ppm Na concentrations the mobility lies between $5\text{x}10^{-13}$ and 10^{-15} $m^2V^{-1}s^{-1}$ [58]. The values taken for the parameters are: $\mu_{Na} = 2 \cdot 10^{-15}$ $m^2V^{-1}s^{-1}$, $\mu_H = 10^{-3}\mu_{Na}$, $\rho_{Na} = 5 \cdot 10^{-22}$ m^{-3} and $\rho_H = \rho_{Na}$. Figure 3.3

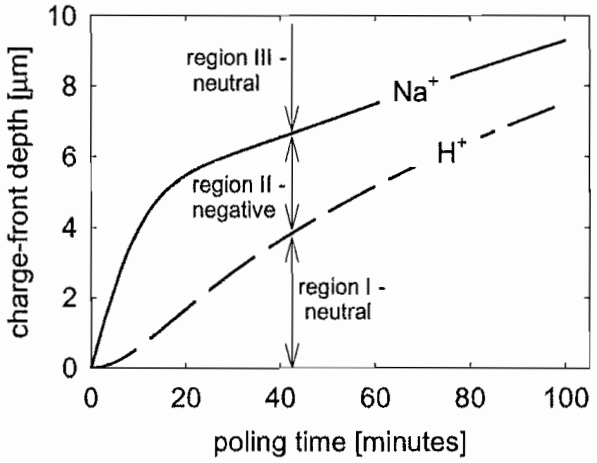

Figure 3.3: Calculated charge-front evolution for both Na^+ and H^+ in a 1 mm thick Herasil glass slide. Migration of the charged ions will create three regions, I, II and III, as indicated. The values taken for the parameters are: $\mu_{Na} = 2 \cdot 10^{-15}$ $m^2V^{-1}s^{-1}$, $\mu_H = 10^{-3}\mu_{Na}$, $\rho_{Na} = 5 \cdot 10^{-22}$ m^{-3} and $\rho_H = \rho_{Na}$.

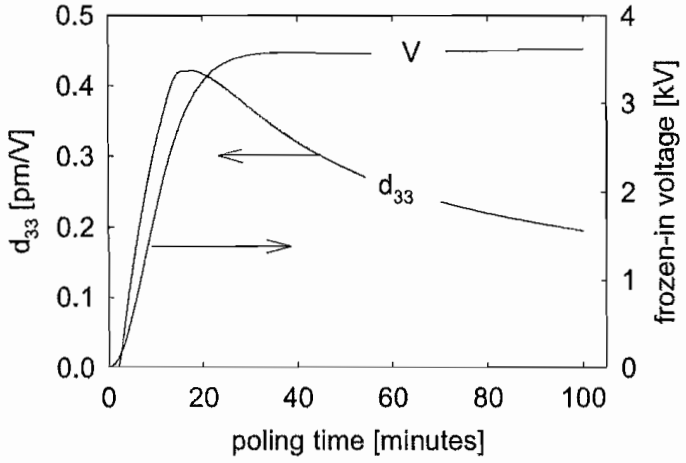

Figure 3.4: Calculated d_{33} and V. The values taken for the parameters are as in figure 3.3.

shows the evolution of the Na^+ and H^+ charge fronts with poling time. Regions I and III are neutral whereas region II is negatively charged and becomes thinner as it moves deeper into the sample. Comparison of figures 3.1 and 3.3 shows how a two-charge model can better explain a continuous growth of the nonlinear depth with poling time and the multiple time scales observed by Alley et al. [58], i.e. an initial fast growth (due to the fast-moving Na^+-ions) followed by a slower growth rate (due to the effect of the low-mobility H^+-ions).

The nonlinear coefficient d_{33} will follow the same evolution of the internal electric field (see eq d_{33}). Figure 3.4 shows the calculated d_{33}, using eq. 2.1 and $\chi^{(3)} = 4 \cdot 10^{-22}\ m^2/V^2$ [31]. Once again, a one-charge model predicts a monotonic increase to maximum value whereas it is well known that the nonlinearity decreases for long poling times [43]. Also shown is the time-evolution of the internal frozen-in voltage, V, obtained integrating the internal electric field across the depletion region. As expected, the total voltage drop inside the glass increases with poling time reaching a maximum value which is very close to the applied 4 kV.

3.3 Measurements

3.3.1 Nonlinearity evolution during thermal poling and dependence on sample thickness

In order to assess the nonlinearity evolution experimentally, samples of different thickness (S) were thermally poled for various poling times. The silica-glass samples were Herasil 1 grade (from Heraeus) with sample thickness $S = 1$, 0.5 and 0.1 mm. Thermal poling was performed at 270^oC in air by applying a constant voltage (V) of 4kV, using Al-evaporated electrodes, for seven different times - 2, 5, 10, 20, 30, 45 and 90 minutes. The samples were subsequently cooled to room temperature with the voltage still applied. Cooling from 270^oC to 200^oC (when poling effects become negligible) takes ~ 40 seconds.

L was obtained using the noncollinear Makers fringe technique (NCMFT) described in chapter 2. Once L is known the nonlinear coefficient is found by normalising the collinear SH with respect to that from a reference sample (quartz) and assuming that the tensorial components of the nonlinearity d_{33} and d_{31} are related to each other by $d_{33} = 3d_{31}$. All measurements were made one hour after poling and then repeated a week later without observing any significant variation in the measured L or d values. Figure 3.5 shows the observed evolution of the nonlinear coefficient d_{33}. The lines are only a guide for the eye: a fast initial increase is followed by a significant decrease to a final value which is roughly 50% smaller than the peak-d_{33}. Furthermore, the poling times for which the peak-d_{33} values are observed decrease with decreasing S. These results can be explained assuming that thermal poling relies on the multiple-charge carrier process described above. Most importantly,

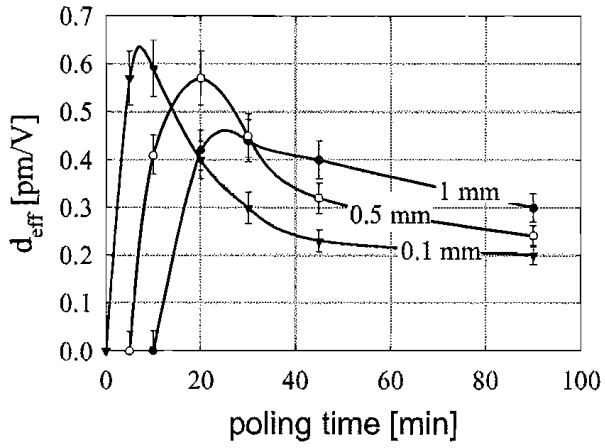

Figure 3.5: Experimental values for the nonlinear coefficient (d_{33}) against poling time for samples of different thickness (S): $S = 0.1$ mm - full circles; $S = 0.5$ mm - empty circles; $S = 1$ mm - full triangles. The lines are only a guide for the eye.

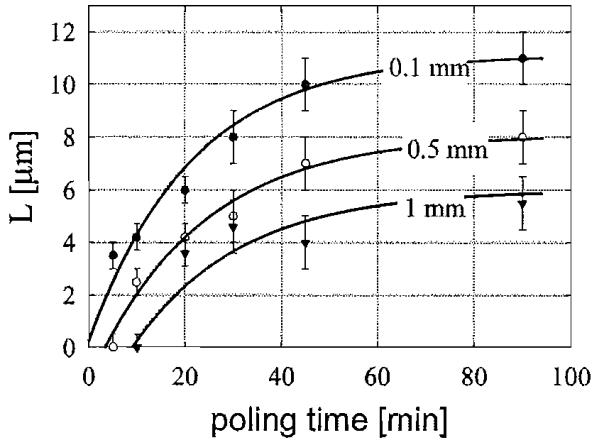

Figure 3.6: Experimental values for the nonlinear thickness (L) against poling time for samples of different thickness (S): $S = 0.1$ mm - full circles; $S = 0.5$ mm - empty circles; $S = 1$ mm - full triangles. The lines are the best stretched-exponential fits for the experimental data.

there is a strong dependence on S due to the different electric-field values inside the sample. Fig.3.5 also shows that there seems to be a minimum poling time below which no SH is observed. This minimum poling time is smaller than 40 seconds (necessary to apply the voltage and cool the sample) for $S = 0.1$ mm but increases to 5 minutes for $S = 0.5$ mm and to 10 minutes for $S = 0.1$ mm. Furthermore, poling at a higher temperature (e.g. $280°C$) resulted in a shift of these threshold times to smaller values (2 minutes for $S = 0.5$ mm and 5 minutes for $S = 0.1$ mm). These results may be explained by assuming that the time required for a charge distribution to form, such that SH generation can occur, depends on both temperature and S. By raising the temperature (i.e. ionic mobility) or decreasing S (i.e. increasing the applied electric field) the necessary (for SH generation) charge distributions are achieved for smaller poling times.

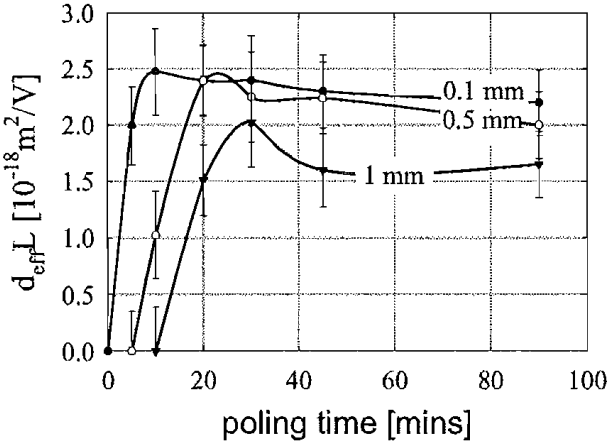

Figure 3.7: Product $d_{33}L$ of the measured nonlinear coefficient and thickness against poling time for three sample thicknesses: $S = 0.1$ mm - full circles, $S = 0.5$ mm - empty circles, $S = 1$ mm - full triangles. The lines are only a guide for the eye.

Figure 3.6 shows the evolution of L for the same samples of fig.3.5. The well-known continuous increase in L is observed (see e.g. [43]). The lines show the best fits for which stretched-exponential functions were used, i.e. functions of the form

$$f(t) = f(0) + \alpha(1 - e^{-\beta t}) \tag{3.3}$$

where $f(0) + \alpha = f(\infty)$ is the saturation value and β is the growth rate. The values which gave the best fits for L are shown in table 3.1. All experimental L values are well described by eq. (3.3). The most important feature of figure 3.6 is the marked dependence on sample thickness. As can be seen, β_L is the same for all S, indicating that the nonlinearity-formation mechanism is the same for all sample thicknesses. Once again, using the described ion-migration model it was possible to establish that the different dynamics and values observed for different S may be ascribed to the different electric fields inside the samples.

Figure 3.7 shows the product $d_{33}L$ against poling time. The solid curves are a guide for the eye. The growth rates vary according to the sample thickness but the saturation value is roughly the same ($\simeq 2.4 \cdot 10^{-18}$ m^2/V) for all S. This value may be used to estimate the sample $\chi^{(3)}$ using eq (2.1) and assuming that all the applied 4 kV voltage drops across the depletion region and remains constant. In this case we find $\chi^{(3)} = 4 \cdot 10^{-22}$ m^2/V, in good agreement with values measured in poled fibres [31].

The importance of these results lies not only in the deeper understanding acquired of the thermal poling process but also in the specification of the poling parameters (temperature and time) necessary for an enhanced efficiency of the SON in waveguide devices. Indeed, the overlap between the nonlinear and waveguiding regions, along with the d_{33} optimisation, is of major importance. This issue will be

discussed in more detail in chapter 4.

$S \longrightarrow$	1 mm	0.5 mm	0.1 mm
$f(0)$ (μm)	-3.1	-1.26	0
α_L (μm)	9	9.39	10.87
β_L (s^{-1})	0.045	0.044	0.046

Table 3.1: Values for the parameters α and β used in the fitting function $f(0) + \alpha(1 - e^{-\beta t})$ for L for all three sample thicknesses (S).

3.3.2 Surface-voltage measurements

In figure 3.4 we show the calculated evolution of the internal frozen-in voltage. The internal voltage is difficult to measure experimentally but the sample surface-voltage can be directly measured using a fieldmeter [65]. We used a "field-mill" instrument, JCI 140CF, which has a conducting sensing surface on which the electric field (given by the voltage gradient between the sample surface and the earthed fieldmeter) to be measured induces a charge. The "field-mill" is so called because it uses an earthed chopper to modulate the electric field at the sensing surface thus improving sensitivity and eliminating the need to "zero" the instrument before each measurement (as has to be done with the simpler induction probe meters). The field meter was initially calibrated by placing the same electrode used for thermal poling at a 1 cm distance with 1 kV applied. We noticed that thermally poled samples show a high (kV) surface voltage straight after poling and that this voltage decays slowly with time, most probably due to the formation of a shielding surface film (made of charged atmospheric particles and ions). Reheating of the sample was seen to regenerate this externally measurable voltage. Therefore we first characterised this regeneration process. A 1 mm thick Herasil glass slide poled at 280^oC, 4 kV for 10 minutes, was heated at successively higher temperatures and both anode and cathode-surface voltages were measured. Figure 3.8 shows the results of these measurements. Both the anodic and the cathodic surface voltages follow the same behaviour: below 150^oC no voltage is measured but above this temperature the isolating film evaporates "releasing" the internal electric field. For temperatures higher than 200^oC the signal decreases rapidly and disappears completely above the poling temperature (280^oC). This decay at high temperatures is also observed in the SH signal and is due to ions migrating under the effect of the high temperature and internal electric field.

Figure 3.10a) shows the expected electric field from a free poled glass sample. When the cathode is earthed and the (earthed) field-meter is placed above the anode sample face then the measured electric field and surface potential will be positive, as in b), and negative values are found when the anode sample face is

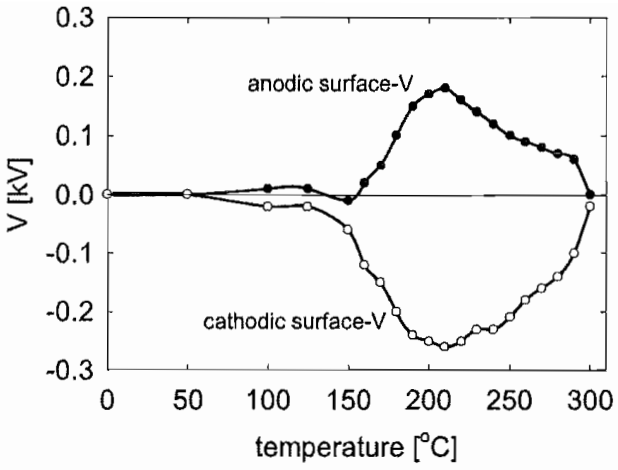

Figure 3.8: Measured surface voltage against heating temperature from both anode (positive values) and cathode-surface (negative values) from a 1 mm thick Herasil 1 sample poled at 280^oC, 4 kV, 10 minutes.

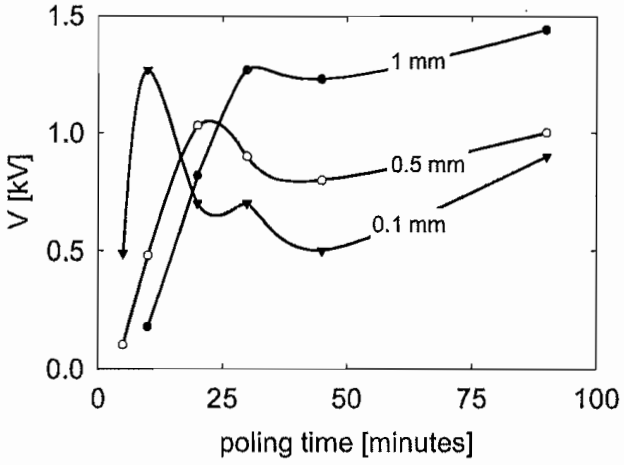

Figure 3.9: Measured anodic surface-potential for poled Herasil samples of different thickness.

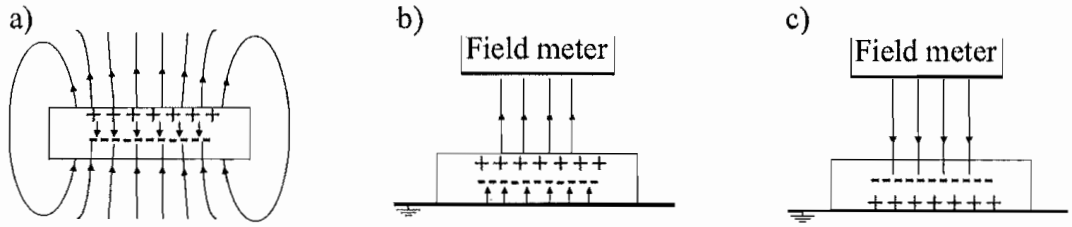

Figure 3.10: a)-configuration of the electric field formed by a free poled glass sample. b)-configuration of the electric field measured by the field-meter when the the cathode face is earthed and c)-when the anode face is earthed.

earthed, as in c). Such a charge distribution (positive layer at the anode and negative layer nearer to the cathode) confirms previously reported measurements using a Laser Induced Pressure Pulse (LIPP) method [66]. Moreover, the surface voltage may be directly related to the internal frozen-in voltage. Indeed, when one of the

faces of the sample is earthed then only the charge distribution nearest to the field meter gives a contribution to the surface potential which may, in a first approximation, be considered equal to the actual internal voltage. In other words, the total internal voltage is given by $V = (\text{anodic surface-}V) - (\text{cathodic surface-}V)$. In our samples we also found $|\text{anodic surface-}V| \sim |\text{cathodic surface-}V|$ so that we may write $V \sim 2 \cdot (\text{anodic surface-}V)$. Taking the peak values measured from figure 3.9 we can see that the frozen-in voltage is nearly equal to the externally applied poling voltage.

In order to measure the surface voltage from the poled samples characterised using the NCMFT (section 3.3.1), we heated the samples to 210^oC for two minutes and measured the anode surface voltage as described above. The results are shown in figure 3.9. The voltage rises with poling time as expected (see figure 3.4) but also shows a marked dip before increasing once again. Furthermore, the dip is deeper for thinner samples. This behaviour indicates that there are different processes occurring during the thermal poling process. Indeed it has already been suggested that during the poling process a depleted region forms in which the electric field is of the same order of the silica dielectric breakdown value [55, 43], i.e. 10^9 V/m [64, 52]. On the basis of our results we suggest that during the first minutes of poling a fast Na^+ migration takes place that creates a strong depletion region, a peak in the internal (and surface) voltage and nonlinearity and finally an avalanche electronic conduction near the anode surface. This avalanche of electrons partially neutralises the internal voltage drop (thus the dip in the measured surface voltage) and finally wears out, allowing the voltage to start increasing once again. This model is further supported by the marked dependence on sample thickness. The thicker samples have a lower externally applied field so that the internal electric field shall also be weaker and the electronic migration less pronounced (thus the smaller dip in the voltage for thicker samples).

These measurements are of great importance because they represent the first measurement of the actual frozen-in voltage, they highlight the presence of an electronic contribution to the poling process and, most of all, they show that the nonlinearity that can be induced in silica glass seems to be intrinsically limited by dieletric breakdown. It is also clear that the two-ion model described in the first part of the chapter provided us with some useful information but is also rather over-simplified. Electronic conduction should be taken into account in future models although this may be rather difficult due to the highly nonlinear nature of such migration under electric fields of the same order of the dielectric breakdown limit.

Chapter 4

Thermal poling of silica waveguides

4.1 Introduction

In the general introduction I gave an overview of the status of research on thermal poling and of its importance for optical telecommunication devices. The general idea is that thermal poling will find applications mainly in fibre-based components: in bulk and planar waveguides other materials such as $LiNbO_3$ are able to cover most needs for a second order nonlinearity. As we showed in chapter 3, the nonlinearity induced by thermal poling has a rather limited extent inside the glass, typically less than 20 μm for poling in air atmosphere. This limitation may become an issue when poling waveguides if the nonlinearity does not overlap with the core region. Indeed, as already pointed out in the general introduction, the effective nonlinearity in a waveguide is given by

$$d_{\text{eff}} = \frac{A_{\text{OVL}}}{m\pi} \left| \int \int f_{\omega}^{2}(x,y) d(x,y) f_{2\omega}^{*}(x,y) \mathrm{d}x\mathrm{d}y \right| \tag{4.1}$$

and thus depends strongly on the overlap between the nonlinear layer and the two (fundamental and SH) propagating modes. Table 1.2 shows that some good results have been obtained in germano-silicate fibres indicating that, to some extent, the nonlinearity does cover the core region.

There are, however, other rather concerning results which have emerged during the last years. Indeed, it has proved very difficult to obtain efficient SH conversion from the fundamental LP_{01} to the SH LP_{01} mode [15]. In particular, three sets of fibres, each with a different NA (0.32, 0.19 and 0.065) were periodically poled (so as to create a nonlinear grating) and then tested [15]. However efficient $LP_{01} \rightarrow LP_{01}$ SH generation was observed only in the NA=0.19 set. The NA=0.32 set showed a marked $LP_{01} \rightarrow$SH-LP_{21} coupling between the pump and SH wavelength with

no measurable LP_{01}→SH-LP_{01} conversion and the NA=0.065 set showed efficient LP_{01} →SH-LP_{11} conversion (see figure 4.2).

4.2 Thermal poling in Ge-doped planar waveguides and fibres

It has already been suggested that the generation of higher order SH waveguide modes and the low d-values observed in our fibres can be explained by supposing a non-uniform nonlinear layer in the fibre, most probably with a hole in the core region ([15]). In other words, it would seem that the germanium in the core is affecting in some way the poling process. In order to study more closely the problem we have thermally poled a series of planar waveguide structures such as that shown in figure 4.1. These waveguide structures, fabricated by D.W.J. Harwood (ORC,

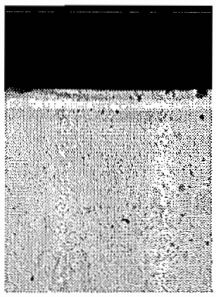

Figure 4.1: Planar waveguide structure used for the investigation of the effect germano-silicate layers on thermal poling. The synthetic-silica overcladding, the germano-silicate core and the underlying synthetic-silica layer are each 5 μm thick. The structure is made on a Herasil, $\simeq$200 μm thick, substrate.

Southampton University), have three layers deposited by chemical vapour deposition on a thick (200 μm) low-grade silica substrate. The layers are: a synthetic silica overcladding, a germano-silicate core and an underlying synthetic-silica layer and all three are of the same thickness. The samples all had an NA=0.1 and were fabricated with three different thicknesses, i.e. 20 μm, 5 μm and 2.5 μm (single layer thickness). They shall be referred to simply as 20 μm-, 5 μm- and 2.5 μm-waveguides, respectively. All samples were poled in vacuum. As a general rule, thermal poling in vacuum gives rise to deeper nonlinear regions compared to thermal poling in air [43] and typically the nonlinear thickness (L) will be greater than 20 μm even for short (5-10 minutes) poling times. First we poled three 20 μm-waveguide samples at 310^oC, 4 kV for 10, 30 and 70 minutes respectively. The samples were then characterised using the one-beam Makers fringe technique [41]. For clarity, all the results are sumarised in table 4.1. We found $L = 22$ μm and $d_{33} \simeq 0.1$ pm/V in all three samples. This result is interesting for many reasons. Firstly, $L = 22$ μm implies that the nonlinear region is concentrated in the overcladding. However the d_{33}-value is much higher than that expected from synthetic-silica which is

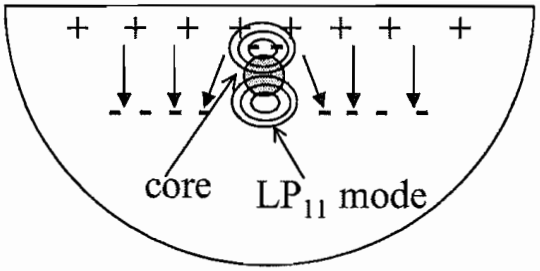

Figure 4.2: Poled D-shaped fibre with maximum conversion efficiency from the fundamental LP_{01} mode to the SH LP_{11} mode. Also indicated is a possible frozen-in charge distribution that could account for this and other results described in the text.

waveguide type	poling temp. (^oC)	Voltage (kV)	time (mins)	layer depth (μm)	L (μm)	expected L (μm)
20 μm	310	4	10	20	20 ± 2	30
20 μm	310	4	30	20	22 ± 2	35
20 μm	310	4	70	20	20 ± 2	40
5 μm	280	4	10	5	5 ± 1	30
5 μm	280	4	60	5	6 ± 1	38
2.5 μm	280	4	20	2.5	8 ± 1	32
5 μm	320	8	20	5	38 ± 2	-
5 μm	320	4	20	5	26 ± 2	-

Table 4.1: Nonlinear thickness (L) measurements on poled germano-silicate waveguides. The L-values were obtained using the HF-technique: they are to be compared with the expected values, i.e. with values obtained in bulk Herasil glass.

very similar to Suprasil-grade glass and normally shows a nonlinearity one order of magnitude smaller than the value we measured. This enhancement of the induced nonlinearity may be due to a possible contamination during deposition. The most interesting result, though, is the constant L and d_{33}-values which are independent of poling time. This can be only explained by assuming that the germano-silicate layer is blocking the growth of the nonlinear region. This assumption was further verified by poling two 5 μm-waveguides at 280 ^oC, 4 kV for 10 minutes. In these samples the overcladding layer is only 5 μm thick and indeed our measurements gave $L = 5$ μm with a high nonlinearity ($d_{33} = 0.3$ pm/V) in both samples. This proves that the germano-silicate layer in some way blocks the ion-migration process. We then poled a 2.5 μm-waveguide sample at 280^oC, 4 kV for 20 minutes. In this sample we found $L = 8$ μm: the nonlinearity extends through the cladding, the guiding core, the underlying synthetic silica layer and into the Herasil substrate. L is still definitely smaller than the expected 32 μm value but nevertheless this result does provide a possible solution to the problems encountered so far. We may speculate that it is a Ge-induced network modification which is inhibiting Na-migration and that poling at a higher temperature and/or voltage could increase

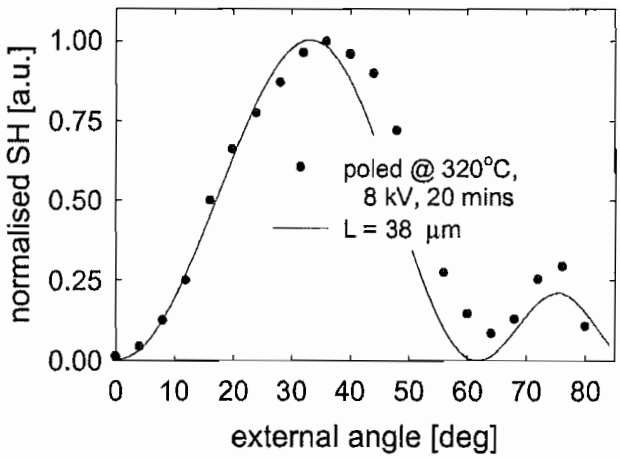

Figure 4.3: One beam MFT measurement on a 5 μm-waveguide, poled at 320^oC, 8 kV for 20 minutes. The nonlinear thickness is 38 μm.

the nonlinearity depth. Indeed, a 5 μm-waveguide was poled at 320^o with 8 kV for 20 minutes and a nonlinear depth of 38 μm was measured (see figure 4.3). Another such sample, poled at 320^o with 4 kV for 20 minutes, gave a depth of 26 μm so we may conclude that higher poling temperatures do indeed allow the nonlinearity to penetrate the core layer. The samples were all poled in vacuum and if one ignores the limited number of H^+ ions present in the hydrated surface (the only source of H^+ ions when poling in vacuum) then a one-charge ion migration model (described in chapter 3) gives a rough estimate of the nonlinear-depth dependence on poling voltage, i.e. $L \propto \sqrt{V}$. This relation is verified by the two samples poled at 4 and 8 kV and indicates an unhindered ion migration through the Ge-doped layer. This result is very promising but the fibre geometry is rather different and the Na ions may still follow a path which moves around the core rather than through the core, even at these higher temperatures and voltages. We therefore prepared a series of fibre samples which can be divided into two sets (see figure 4.4):

1. the NA=0.32 fibre, with a 10 μm separation between the two electrode holes and less than 2 μm between the anode and the core;
2. the NA=0.1 fibre with a 160 μm separation between the two electrode holes and 12 μm between the anode and the core.

After thermal poling under the conditions shown in table 4.2 we measured the electro-optic coefficient (r) using a heterodyne Mach-Zender interferometer designed and developed at Kent University by C. Pannell et al., shown in figure 4.5. A He/Ne laser is used for the initial alignment whereas, for the actual measurement, the 1550 nm output from a diode laser is split into the two arms of the interferometer with 90% of the power in the sample arm (which has the highest losses) and 10% in the reference arm. Polarisation controllers (PC) ensure that the polarisation is

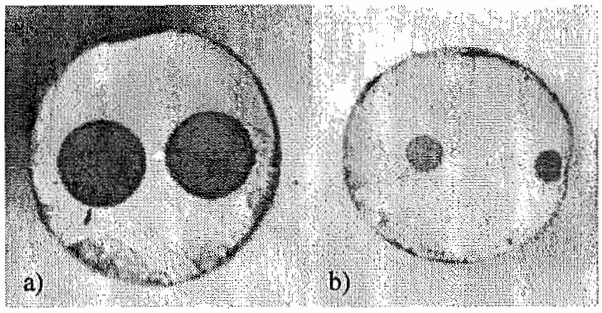

Figure 4.4: Twin-hole fibres used for electro-optic coefficient measurements. The electrode spacing in the NA=0.32 fibre (a) is 10 μm and 160 μm in the NA=0.1 fibre (b).

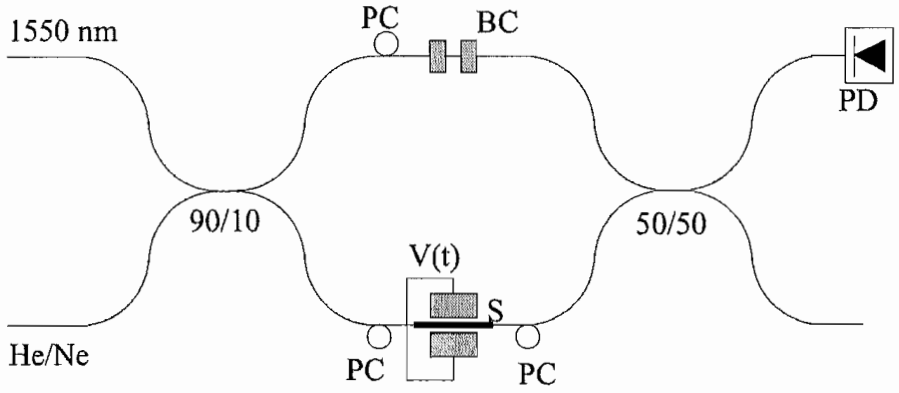

Figure 4.5: Experimental layout of the heterodyne Mach-Zehnder interferometer used at Kent University for our electro-optic measurements. PC - polarisation controller, BC - Bragg cells giving the 50 kHz carrier frequency in the reference arm, He/Ne - visible laser used for alignment, S - fibre sample, PD - photodiode, V(t) - electrodes supplying the sinusoidal voltage, V(t), to the sample.

maintained in all stages. The reference arm is modulated by two inverted Bragg cells (BC) which have their modulating frequencies slightly offset (by 50 kHz) so that the overall effect is a 50 kHz frequency shift of the optical carrier. The sample, in the other arm of the interferometer, is placed between two electrodes and modulated with a sinusoidal voltage with a peak value of the order of 100 V and a frequency in the 3-5 kHz range. The two arms are recombined with a 3 dB coupler and the signal is measured with a photodiode connected to an RF spectrum analyzer. The ratio between the peak value of the carrier frequency (50 kHz) and the sidebands (at 3-5 kHz to either side of the carrier frequency) is directly related to the electro-optic coefficient. The underlying theory of this experiment is explained in more detail in appendix B and the results of the electro-optic measurements are shown in table 4.2. The r-coefficient is related to d by the relation ([9])

$$d = \frac{n^4}{4} r \tag{4.2}$$

NA	poling temp. (C)	voltage (kV)	time (mins)	EO-coeff. (pm/V)
0.32	280	4	5	0.044
0.32	280	4	7.5	0.062
0.32	280	4	10	0.082
0.32	280	4	12.5	0.06
0.32	280	4	15	0.046
0.32	280	4	20	0.039
0.32	270	4	10	0.18
0.32	350	6.8	10	0.058
0.32	400	4	10	0.06
0.1	280	4	10	0.014
0.1	280	4	20	0.023
0.1	280	4	40	0.029
0.1	280	4	60	0.022

Table 4.2: Electro-optic coefficient measurements, made on fibres thermally poled under various conditions.

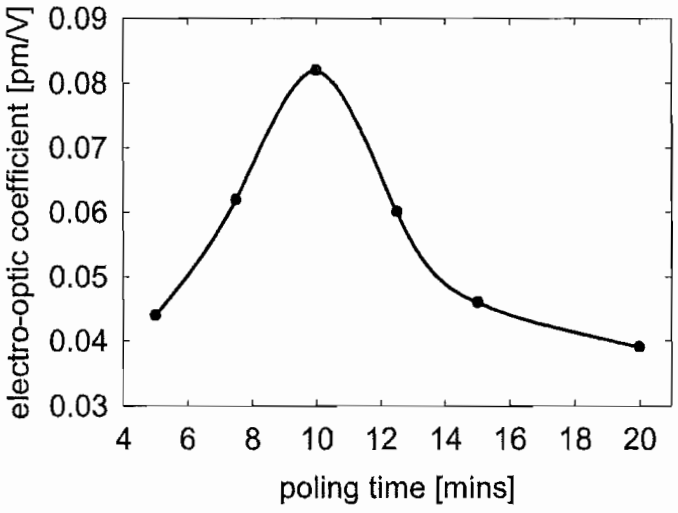

Figure 4.6: Measured electro-optic coefficient against poling time, for thermally poled twin-hole NA=0.32 fibres. Poling was carried out at 280^oC and 4 kV.

where n is the refractive index (in silica glass $n^4/4 \simeq 1.1$). Figure 4.6 shows the electro-optic coefficient for the NA=0.32 fibres poled at 280^oC and 4 kV for different times. The dependence on poling time is very similar to that found in bulk silica glass (see chapter 3) and a peak value of nearly 0.1 pm/V is obtained after 10 minutes poling. However, it is also important to notice that higher poling temperatures and/or voltages did not increase the fibre nonlinearity (on the contrary, the highest value was obtained at a slightly lower temperature of 270^oC). Furthermore, the NA=0.1 fibre has always given lower nonlinearities. The main difference between the two sets of fibres which seems to be influencing the poling process is the distance between the electrodes and the core. As confirmed in planar waveguide

structures, it is very important that the core lies not more than 2 or 3 μm from the anode. This may be explained by using the two-charge model for thermal poling in air, developed in chapter 3. A very fast initial growth of the depletion region, due to Na^+ migration and extending only a few microns under the anode surface, is observed in the first minutes of poling. Then a much slower migration process, which involves also H^+ ions, takes over. The ions during the fast initial growth have enough energy to penetrate the Ge-doped layer and extend the depletion region, i.e. the nonlinearity, through the core. On the other hand, if the core is too far away to be reached by the depletion region during this phase, then the migrating ions, now slowed down by the in-diffusing H^+, may be blocked at the Ge-doped layer interface. It would therefore seem that whereas in planar waveguides both the anode-core distance and the poling parameters (i.e. temperature and voltage) can be varied to obtain a nonlinear core, in fibres only the anode-core distance is important. This is confirmed by our experimental results and those obtained by others ([32, 33]).

4.3 Thermal poling of holey fibres

There may be other solutions to the problem. For example a different doping element could be used for the core such as phosphorous or tin. The latter is particularly interesting due to the fact that, with respect to germanium, a much smaller concentration of tin is necessary to obtain an NA=0.1 fibre. Specially designed depressed cladding fibres with a pure silica core surrounded by a thick cladding layer of boron or fluorine doped silica could also prove effective. However, a more elegant solution is to use microstructured fibres, also known as photonic crystal fibres or holey fibres. The core is surrounded by a periodic array of holes which create an effective refractive index that is lower than that of the glass centre-rod. In this way, light is guided by total internal reflection as in a normal fibre, but the core and surrounding glass are all made of the same silica and no Ge-doping is required. The outer supporting structure had holes which are typically 30 μm in diameter so that 25 μm electrode wires can be inserted for thermal poling. The internal structure is made from Herasil-grade silica: figure 4.8a) shows an SEM picture of this region. The fibre is multimode but we were able to efficiently couple light into the fibre in such a way that at least 80% of the power was in the fundamental mode, shown in fugure 4.8b). It is important to note that the distance between the core and the nearest outer hole, used to house the anode wire, is 27 μm. If such a large distance were to be used in standard fibres the nonlinearity would not overlap with the core. Moreover the air:silica structure is rather complex and it was impossible to predict if thermal poling, which relies on ionic migration, would take place at all.

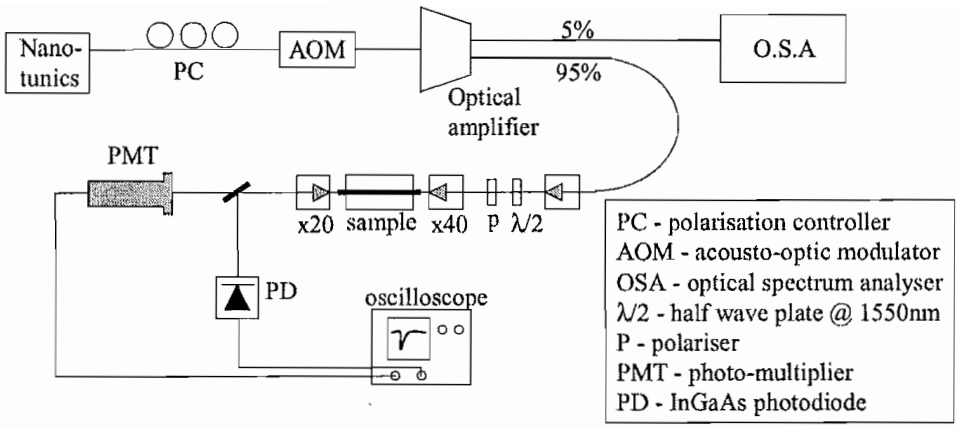

Figure 4.7: Experimental layout used for testing SHG in thermally poled holey fibres.

Thermal poling was carried out in air atmosphere at 280^oC, 4 kV and 30 minutes and the samples were then tested for SHG. The SHG experimental setup is shown in figure 4.7: the CW tunable output from a semiconductor laser (Photonetics Nanotunics) passes through a polarisation controller (PC) and is then modulated in amplitude by an acousto-optic modulator (AOM). The resulting 200 ns pulses (at 1 kHz repition rate) are amplified in an Er^+-doped amplifier, focused into the sample with a x40 microscope objective and collected at the fibre output with a x20 objective. A Fresnel reflection from a glass slide is used to monitor the pulse peak power (measured with a fast InGaAs photodiode) and the SH signal is collected by a photomultiplier tube. The pulses at the fundamental wavelength are eliminated by a broadband RG9 (Schott) filter and by the photomultiplier itself which is insensitive to wavelengths above 900 nm.

The pulses coupled with a 30-40 % efficiency into the fibre had a peak power of

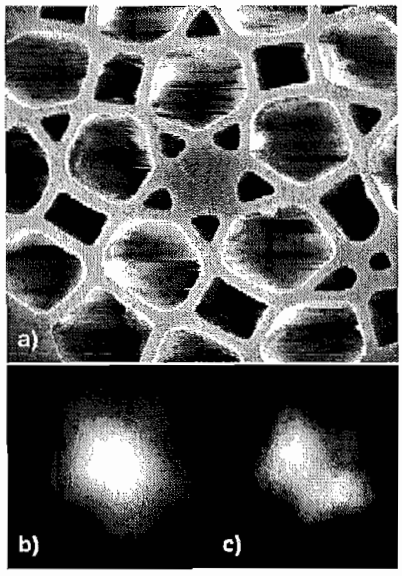

Figure 4.8: a) - core region of the thermally poled holey fibre. b) - mode profile at 1550 nm and c) - at 775 nm.

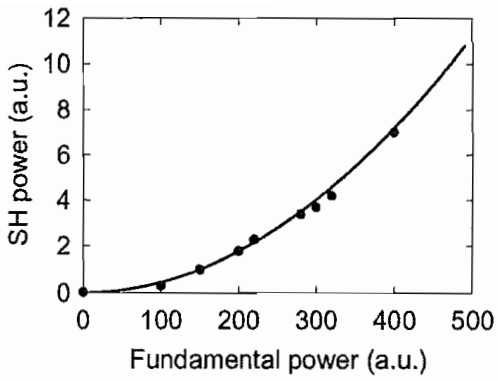

Figure 4.9: Dependence of the second harmonic (SH) on the fundamental power: the points are the experimental data and the solid curve is the best quadratic fit.

$\sim 5\ W$ (measured with the InGaAs photodiode) and an average power of $\sim 1\ mW$. Second harmonic generation was observed in the poled holey fibres and the average conversion efficiency was estimated to be of the order of $10^{-8}/W$. This efficiency is very low but we must bear in mind that the process wasn't phase-matched. Indeed, we poled three different samples and the conversion efficiency varied greatly from one sample to the other. The SH was also polarisation dependent with a ratio, in the measured SH power, of 1:4 between the two orthogonal polarisation states and figure 4.9 shows the quadratic dependence of the SH signal as a function of the fundamental pump power. It is impossible to estimate the actual $\chi^{(2)}$ value on the basis of these results and we therefore measured the electro-optic coefficient. This was done using the heterodyne Mach-Zehnder interferometer described in appendix B and previously used for the characterisation of poled germano-silicate fibres. We found r to be $0.02\ pm/V$. Although this value is lower than that found in germano-silicate fibres, it must be emphasized that this is a first demonstration of thermal poling in such complex structures and that the actual fibres did not have an optimal design for the poling process. Moreover, a systematic study of the poling parameters proved essential for the optimisation of the nonlinearity in germano-silicate fibres and is also necessary in holey fibres.

In general, holey fibres are very attractive for nonlinear applications for a number of reasons in addition to the possibility to use the optimum glass composition in the core:

1. single mode operation can be obtained over a broad band of wavelengths [67]. This is of great importance both for SHG and when pumping a difference frequency generation process at 755 nm with the generated signals in the 1550 nm region.
2. it can also be shown that the fundamental modes at the different wavelengths have a better overlap than in standard fibres. This factor alone will increase

the conversion efficiency by an order of magnitude.

3. very small mode diameters ($\sim 1\ \mu m$) can be achieved, thus greatly increasing the pump intensity and the overall conversion efficiency.
4. the fibre geometry can be tailored so as to minimise dispersion [68] and thus greatly increase (by at least a factor 10) the frequency generation bandwidth. This is very important due to the fact that, as pointed out in the general introduction, the SHG bandwidth in a standard fibre is very small ($\sim$0.2 nm) and any fluctuations in the fibre parameters or environmental conditions will severely limit the conversion efficiency. Furthermore, wavelength conversion of ultra-short pulses require higher bandwidths - the shortest pulse duration which can be converted with a 0.2 nm bandwidth and without actually lengthening the pulse is $\sim$ 40 ps.

In conclusion, in this chapter we have analysed the problems encountered in poling optical waveguides. The low effective nonlinearities found in fibres have been attributed to a greatly reduced or completely absent nonlinearity in the core region. Studies in planar waveguides showed that this problem can be overcome by poling at higher temperatures and/or voltages and by placing the core region very close to the poling anode. Indeed, the latter solution proved very efficient and allowed us to measure an electro-optic coefficient of 0.12 pm/V in an NA=0.32 fibre which had the core less than 2 μm away from the anode. Another solution to the problem could be to use fibres with a pure silica core, e.g. holey fibres. Thermal poling of holey fibres has been demonstrated for the first time and is attractive not only for the possibility to use the desired glass composition in the core but also for other features such as endless single mode operation and a greater bandwidth for frequency generation processes.

Chapter 5

Second-order nonlinearity enhancement in silica glass

5.1 Introduction

In chapter 3 we described how the induced nonlinearity in silica-glass may be optimised by using the right poling parameters, i.e. temperature, voltage and poling time. Research has also been carried out to search for ways to enhance the nonlinearity by modifying in some way the actual glass.
As discussed in chapter 3 the main ion species involved in the thermal poling process is Na^+. It therefore seems reasonable that a moderate increase in the concentration of this ion may enhance the nonlinearity. Experiments carried out towards this end are described in section 5.2 of this chapter.
Section 5.3 describes nonlinearity enhancement through UV-treatment.

5.2 *Na*-injection

We investigated the possibility to increase the induced nonlinearity by injecting ions from soda-lime glass into the poled sample. The steps followed are:

- maintaining the same configuration used for poling, a soda-lime glass slide was placed on top of the sample (figure 5.1). The voltage used was still 4 kV but the temperature was 320°C and the process time varied from 40 minutes to 4 hours. As expected, the ion injection cancelled out any SHG induced during the first step. The current measured passing through the sample was in all cases very high: between 100 μA and 200 μA. It is worth noting that after injection all samples showed a superficial white deposition on the cathode side. This behaviour is very similar to that observed during soda-lime glass poling ([69]).
- All samples were then poled as in the first step. The initial current was still very high ($\simeq$ 1 μA) decreasing to $\simeq$ 100 nA

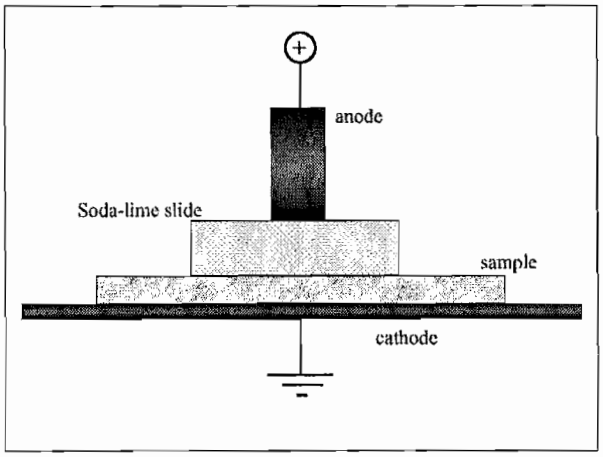

Figure 5.1: Experimental layout for field assisted ion-injection from soda-lime glass into Suprasil or Herasil glass samples.

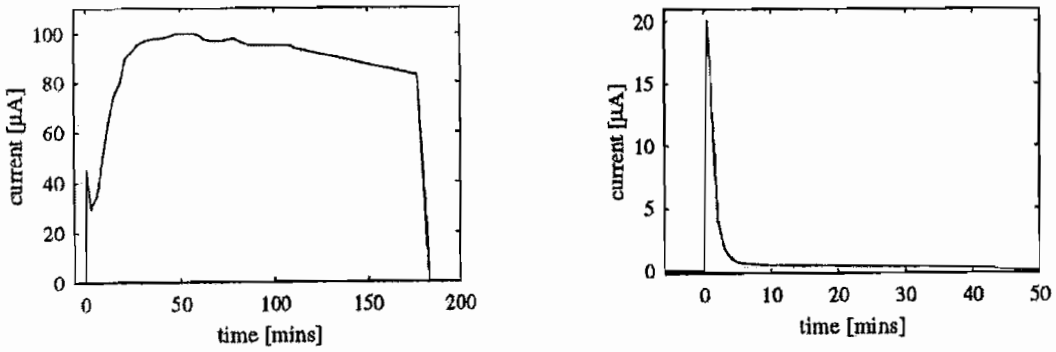

Figure 5.2: The graph to the left shows a typical current vs time dependence during ion-injection (@ 300°C, 4 kV) and, to the right, during poling (@ 275°C, 4 kV). The sample, 070999C, was a 0.2 mm thick Herasil-silica slide.

It is worth noting that this treatment was repeated on both un-poled and already poled glass without noticing but no difference in the final behaviour was observed. The procedure was repeated on both Suprasil and Herasil samples: a general two-fold increase in the second harmonic was always observed in 1 mm thick sample and little or no enhancement in thinner samples (0.1 and 0.2 mm). The Herasil 1 mm samples showed a nonlinearity amplitude similar to that seen in 0.1 mm samples whereas Suprasil showed, as Herasil, a two-fold increase in the nonlinearity that was, however, still 10% of the highest value attainable with Herasil. The high current values observed in the final poling step show that some of the ions remain trapped in the bulk therefore increasing the sample's conductivity. Due to the high mobility of Na ions in glass and the similarity of the injected sample behaviour to that of soda-lime glass (for example the high current values and the white deposition) we can conclude that the ions involved are mainly Na ions.

It is worth noting that the ion injection did not appear to act uniformly. Most

samples showed an overall increase in nonlinearity with some small μm size grains showing a 3 times (in one case four times) increase. The samples were checked with a microscope but no visual evidence of a granular structure was found. The nonlinearity in the "grains" was very unstable and decayed along with the whole average nonlinearity. After 48 hours the situation for the samples poled after Na-injection became similar to that of samples poled without any injection.
These results may be explained by noting that the ion injection uniformly lowers the glass resistivity (as is obvious from the high current values measured during injection and the first minutes of the final poling step). However, during the final poling step the depletion region rapidly forms and looses all memory of the ion injection. The undepleted region still has a lowered resistivity due to the bulk injected ions that haven't moved out of the glass (i.e. the depleted region will have a higher resistivity) so a higher electric field (i.e. second order nonlinearity) will be stored in the depleted region.
Unfortunately the enhancement is rather unstable and an immediate application of this effect isn't forseeable.

5.3 Thermal annealing and UV-treatment of Suprasil glass

Suprasil is typically the silica-glass with the highest purity commercially available and is very similar to the synthetic silica which forms the cladding in standard telecom fibres. The main difference between the two glasses is the OH content which in Suprasil can be as high as 600-1000 ppm whereas it is kept as low as possible in silica fibres. The main aim of the project is to produce a poled fibre with a high second-order nonlinearity. However it is well known that Suprasil grade silica typically gives a nonlinearity that is 10% of that in Herasil. For this reason

glass type	annealing 900^oC, 2 hrs	UV (mJ/cm^2)	shot #	E (J)	poling (mins)	L (μm)	d_{33} (pm/V)
Herasil 1	x	x	x	x	10	4	0.32
Herasil 1	x	55	10^3	28	10	4.2	0.37
Suprasil 1	x	55	10^3	28	10	-	-
Suprasil 1	x	55	10	0.28	10	-	-
Suprasil 1	✓	80	10^3	40	10	4	0.3
Suprasil 1	✓	80	10^4	400	20	4.2	0.44
Suprasil 1	✓	x	x	x	10	-	-

Table 5.1: Summary of results obtained with thermal annealing and UV treatment in Suprasil 1 and Herasil 1 glass slides. E is the total incident UV-energy delivered from a pulsed excimer laser at 244 nm, # the number of shots at 20 Hz repitition rate, UV the single pulse intensity. Poling was carried out at 280^oC, 4 kV for the indicated time. L and d_{33} are the measured nonlinear thickness and coefficient respectively. The "-" sign indicates that there was no detectable SH.

all the fibres we have tested so far had a cladding especially made with Herasil grade glass. In the past thermal poling has been carried out on thermally annealed Suprasil finding an increase to Herasil values [70]. This enhancement was ascribed to the creation of non-bridging oxygen hole centers which increase when hydrogen is driven out (by thermal annealing) of the OH-rich glass. This would also explain why no increase was observed in Herasil which has a much lower (200 ppm) OH content.

On the other hand, it is well known that UV-light, typically at wavelengths shorter than 300 nm, interacts with site defects thus modifying the glass. This kind of interaction is typically used for creating permanent refractive-index changes.

A series of Herasil and Suprasil-grade silica plates were thermally annealed in air at 900^oC and/or UV-exposed (using a 248 nm excimer laser) before being thermally poled. Table 5.1 is a summary of the results. No increase in the nonlinearity is observed after thermal annealing and/or UV-treatment in Herasil glass. It is also obvious that thermal annealing or UV-exposure alone did not produce a significant enhancement of the nonlinearity in Suprasil glass. However, Suprasil glass shows a surprisingly high nonlinearity after both thermal annealing and UV exposure. The L and d_{33} measured values are equivalent to those found in Herasil glass (see also chapter 3). There is no immediate explanation for this enhancement which is very probably related in some way to the creation of free H^+ charges through interaction between UV-light and previously thermally-enhanced glass defect states.

Suprasil samples have also been hydrogen-loaded but no enhancement was observed even after UV-exposure. This could indicate that if the presence of H^+ is indeed the main factor then, in order to be effective, the ions must originate from bonded states (for example with O) and not from non-bonded interstitial states as is the case with H^+ introduced by hydrogen loading.

The main application of such a UV-induced enhancement will be found in pure-silica core fibres. As described in chapter 4, in order to observe d_{33} values in fibres of the same order of those in bulk glass it may be necessary to use fibres with a pure silica core surrounded by a depressed cladding (e.g. holey fibres or boron/fluorine cladding-doped fibres): the synthetic-silica core fibre can be UV-treated in order to increase the nonlinearity. Furthermore, the contrast between UV-exposed and non-exposed regions is very high and this can be used to directly write the quasi phase-matching grating (using the standard techniques used for writing long-period gratings) before the sample is poled.

Chapter 6

Conclusions and future work

The work described in this thesis has focused on the mechanisms lying behind thermal poling in silica glass, on sample characterisation techniques and on the difficulties encountered in transferring the results obtained in bulk silica glass to silica waveguides.

There still exists a certain confusion in literature regarding the profile and the value of the nonlinearity induced by thermal poling. This is due mainly to the difficulty in resolving nonlinear thicknesses smaller than the SHG coherence length with an all optical measurement, such as the Makers Fringe Technique. For this reason we developed the Noncollinear Makers Fringe Technique, described in chapter 2, which proved invaluable for the characterisation of nonlinear layers as thin as 2 μm. Using this technique it was possible to precisely determine the nonlinearity-formation dynamics (chapter 3) in thermally poled silica glass. In chapter 3 we also show for the first time a direct measurement of the frozen-in voltage. For these measurements we took the same samples used to study the nonlinearity formation dynamics. This gave us a global view of the poling process and allowed us to conclude that in addition to ionic migration, electronic conduction also plays a very important role and is probably the factor limiting (through dielectric breakdown) the nonlinearity value in silica glass.

The study on the nonlinearity formation dynamics allows to optimise the overlap between the nonlinear region and the guiding region in optical waveguides. Indeed, it was using these results that we found the optimum poling conditions for our NA=0.32 fibres obtaining an electro-optic coefficient of 0.12 pm/V, an order of magnitude higher than that from previous experiments (see chapter 4).

However the results outlined in chapter 4 indicate very clearly that the presence of a Ge-doped layer significantly hinders the penetration of the nonlinearity into the glass and that use of a higher poling temperature and/or voltage can reduce this limitation.

Another solution to the problem could be the removal of the Ge-doped layer by

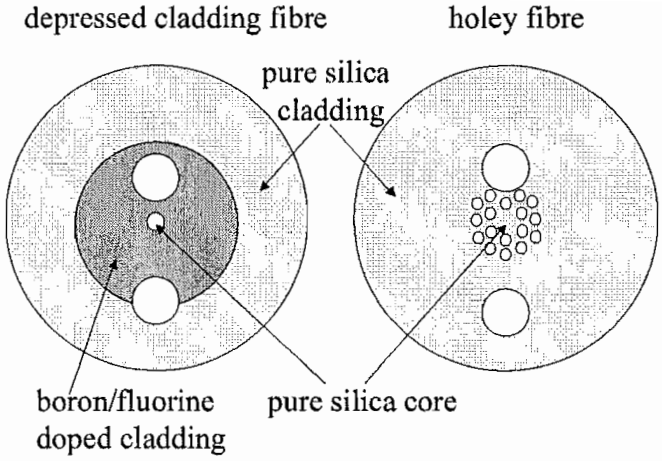

Figure 6.1: New fibres for thermal poling. The fibre to the left has a depressed cladding doped with boron or fluorine whereas the fibre to the right is a holey fibre. The large holes in both fibres, placed either side of the core are for inserting the 25 μm electrode wires.

using a depressed cladding geometry. Figure 6.1 shows two possible fibre geometries which should be considered: the fibre to the left has a pure silica core surrounded by a lower index boron- or fluorine-doped cladding. Problems may arise using boron because the high concentrations needed to obtain an NA$\sim$0.1 render the preform too fragile to drill the holes for the electrode wires. Another possibility (fibre to the right in figure 6.1) is to use a holey fibre: no doping elements are necessary seeing as the cladding refractive index is effectively lowered by the array of holes around the core. In chapter 4 we gave the first experimental demonstration of thermal poling in a holey fibre structure and measured the electro-optic coefficient to be $\sim$ 0.02 pm/V. As we pointed out in chapter 4, holey fibres are able to take advantage in the best way of the potentialities offered by silica-fibre wavelength conversion, i.e. high damage thresholds and high intensities, increased conversion bandwidths, longer interaction lengths and excellent overlap between interacting modes. Both the holey fibres and the depressed cladding fibres also offer the possibility to use a Herasil-grade rod for the core, i.e. the silica glass which so far has given the best results. On the other hand, should the fibres be prepared with a pure synthetic silica core then the results illustrated in chapter 5 show that we can enhance the otherwise very low SON by at least a factor ten by thermally pre-annealing the fibre and then exposing it to UV excimer-laser irradiation at 248 nm before poling. The enhancement occurs only in the UV-exposed regions and we can take advantage of this to write a quasi-phase matching grating (with a period typically in the 50-70 μm range for an NA=0.1 and fundamental wavelength of 1550 nm) using the standard techniques for long period gratings in photosensitive fibres.

Future work should therefore concentrate mainly on the fabrication of an efficient poling-induced nonlinearity in fibres. Most importantly, the initial results obtained in holey fibres should be followed up by new samples with a geometry dedicated to the thermal poling process and a thorough characterisation of ionic migration in such structures. Other fibre geometries and new materials should also be investigated. Of particular interest are new glasses possessing a high resistivity (in order to increase the breakdown threshold during poling) and a high refractive index (in order to maximise the third-order nonlinearity which generally increases with n). Another possibility may also be glasses with a resonant nonlinearity. A recent result obtained by Arentoft et al. ([29]) shows what seems to be a resonant enhancement of the SON after injection of very large amounts of silver into the glass during poling. The absorption losses are very high but this is only an initial result which needs further investigation.

Appendix A

Expressions for NCMFT calculations

The actual calculations for the noncollinear makers fringes technique were carried out using the sample reference system, i.e. a system with the z-axis defined by the sample normal and the x-axis by the sample interface as shown in figure A.1. In

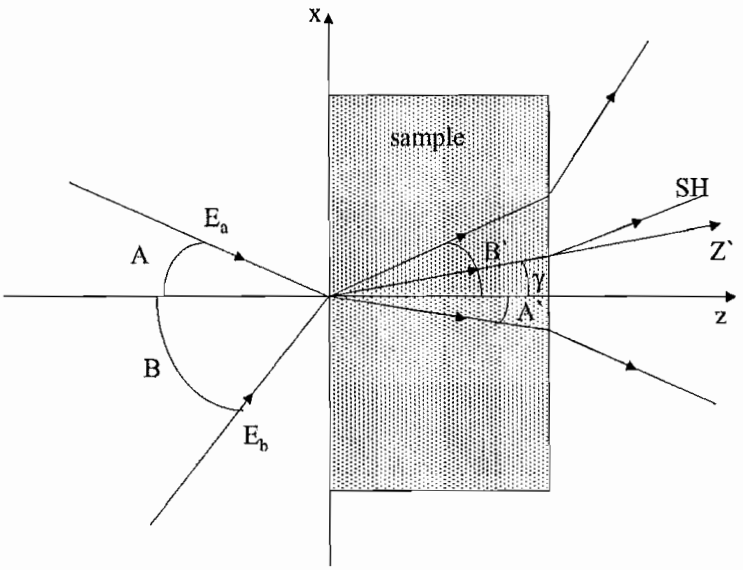

Figure A.1: Angles used for calculating the SH-power angle dependence in the non-collinear Makers fringe technique.

order to avoid confusion the angles and optical beams have been redefined using different names to those used in chapter 2. A and B are the external angles of the two incident fundamental beams with A' and B' their respective internal angles. γ is the SH internal propagation angle and the SH propagation direction also defines the z' axis.

The starting point is eq (2.3). The phase-mismatch is calculated along the second

harmonic propagation direction z' and is thus given by

$$\Delta k = \frac{4\pi}{\lambda}\left(n(\frac{\lambda}{2}) - \frac{n(\lambda)}{2}(\cos(A'-\gamma)+\cos(B'-\gamma)\right) \tag{A.1}$$

where $n(\lambda)$ is given by the Sellmeyer equation (eq (2.6)). The propagation angle of the polarization wave is

$$\delta = \frac{\cos(A')+\cos(B')}{2} \tag{A.2}$$

thus, using the continuity of transversal E and H components at the boundary, the SH propagation angle is

$$\gamma = asin\left(\frac{n(\lambda)}{n(\frac{\lambda}{2})}\sin(\delta)\right) \tag{A.3}$$

The nonlinear film distribution is defined either as a square function or as a gaussian. An truncated gaussian profiled film along x can be written as

$$d_{\text{eff}}(z) = exp\left(-\left(\frac{z-\Delta}{d}\right)^2\right) \tag{A.4}$$

where the offset Δ defines the position of the peak with respect to the air-glass interface.

Finally, integration is carried out along the second harmonic propagation direction and therefore from 0 to $d/\cos(\gamma)$.

As can be seen in equation (2.3), integration is also carried out along x and y in order to include finite volume effects which may change the amplitude of the SH power oscillation. However it is worth noting that this effect can be completely ignored in the y direction: integration in this direction results simply in a constant multiplication factor given by $\int exp(-y^2)$. Therefore, after taking the electric fields as plane waves, equation (2.3) can be written, along the second harmonic propagation direction, as

$$P_{2\omega} \propto C(\alpha)P_\omega^2 \int_{-\infty}^{\infty} \left| \int_0^{\frac{d}{\cos(\delta)}} e^{i\cdot\Delta k\cdot z'} d_{\text{eff}}(z',x)dz' \right|^2 dx \tag{A.5}$$

Changing variables and moving to the sample reference frame, using $z' = \frac{z}{\cos\gamma}$ we obtain the final equation for the SH generation efficiency:

$$\begin{aligned}\eta_{\mathrm{SH}} = \frac{P_{2\omega}}{P_{\omega}^2} &\propto C(\alpha)\int_{-3w}^{3w}\left|\int_0^d e^{i\cdot\Delta k\cdot\frac{z}{\cos(\gamma)}} d_{\mathrm{eff}}(z,x)dz\right|^2 dx\frac{1}{\cos^2(\gamma)} \\ C(\alpha) &= d_{\mathrm{eff}}(\alpha)\cdot\frac{T_{2\omega}(\alpha)}{T_{\omega}^a(\alpha)T_{\omega}^b(\alpha)}\cdot u_a(\alpha)^{-1}\cdot u_b(\alpha)^{-1}\cdot u_{SH}(\alpha)\end{aligned} \tag{A.6}$$

$C(\alpha)$ includes

- The nonlinear tensor projection factor (along the second harmonic propagation direction), which can be calculated using figure (A.1).
  For a material with $C_{\infty v}$ (or C_{4v}, C_{6v}) symmetry the second order nonlinear polarization tensor is defined, using the d tensor as

$$\begin{pmatrix} P_{\hat{x}}^{2\omega} \\ P_{\hat{y}}^{2\omega} \\ P_{\hat{z}}^{2\omega} \end{pmatrix} = \epsilon_0 \begin{pmatrix} 0 & 0 & 0 & 0 & d_{31} & 0 \\ 0 & 0 & 0 & d_{31} & 0 & 0 \\ d_{33} & d_{33} & d_{33} & 0 & 0 & 0 \end{pmatrix} \cdot \begin{pmatrix} (E_{\hat{x}}^{\omega})^2 \\ (E_{\hat{y}}^{\omega})^2 \\ (E_{\hat{z}}^{\omega})^2 \\ 2E_{\hat{y}}^{\omega}E_{\hat{z}}^{\omega} \\ 2E_{\hat{x}}^{\omega}E_{\hat{z}}^{\omega} \\ 2E_{\hat{x}}^{\omega}E_{\hat{y}}^{\omega} \end{pmatrix} \tag{A.7}$$

  with $d_{33} = 3d_{31}$ in a perfectly isotropic medium. P-POL (TM) case:

$$\begin{aligned} E_{\hat{x}}^a &= E_{\omega}^a\cos(A') \quad \& \quad E_{\hat{z}}^a = E_{\omega}^a\cos(A') \\ E_{\hat{x}}^b &= E_{\omega}^b\cos(B') \quad \& \quad E_{\hat{z}}^b = E_{\omega}^b\cos(B') \end{aligned} \tag{A.8}$$

  are the fundamental internal beam components along $\hat{x}$ and $\hat{z}$. Using equation (A.7)

$$\begin{aligned} P_{\hat{x}}^{2\omega} &= 2\epsilon_0 d_{31}E_{\hat{x}}E_{\hat{z}} \\ &= 2\epsilon_0 d_{31}(csh^a + csh^b + E_{\omega}^a E_{\omega}^b\sin(A'+B')) \end{aligned}$$

  and

$$\begin{aligned} P_{\hat{z}}^{2\omega} &= \epsilon_0(d_{31}E_{\hat{x}}^2 + d_{33}E_{\hat{z}}^2) \\ &= \epsilon_0(d_{31}((E_{\omega}^a)^2\cos^2(A') + (E_{\omega}^b)^2\cos^2(B')E_{\omega}^aE_{\omega}^b\cos(A')\cos(B') \\ &\quad + d_{33}(E_{\omega}^a)^2\sin^2(A') + (E_{\omega}^b)^2\sin^2(B')E_{\omega}^aE_{\omega}^b\sin(A')\sin(B')) \end{aligned}$$

  keeping only the mixed (noncollinear terms) and bearing in mind

$$P^{2\omega} = P_{\hat{x}}^{2\omega}\cos(\gamma) + P_{\hat{z}}^{2\omega}\sin(\gamma) \tag{A.9}$$

we have

$$d_{\text{eff}} = d_{31}\sin(A'+B')\cos(\gamma) + d_{31}\cos(A')\cos(B')\sin(\gamma) + \\ + d_{33}\sin(A')\sin(B')\sin(\gamma) \tag{A.10}$$

- the Fresnel transmittivity, $T_{\omega}^{a,b}(\alpha)$, for the fundamental beams at the input face and for the SH, $T_{2\omega}(\alpha)$, at the output face (this factor changes only the maximum position and shape). As above, angles must be taken in the sample ref. frame.
-

$$u_a^{-1}(\alpha)\cdot u_b^{-1}(\alpha)\cdot u_{SH}(\alpha) \tag{A.11}$$

In eq.(2.5) these three terms are all contained in the term "$u(\Theta,\alpha)$". This factor arises from the fact that we measure the average powers outside the medium and that the beam inside the medium has an ellipsoidal cross section so, if the external beam area $A_{ext} = \pi w^2$ then the internal beam area will be

$$A_{int} = \pi w(wu(\alpha)) \tag{A.12}$$

from which follows $I_{int} = I_{ext}u^{-1}(\alpha)$. The integral in eq (A.6) is valid for the internal intensities and can be re-written using the external intensities and multiplying the whole expression by eq (A.11). $u_{a,b,SH}(\alpha)$ are simply given by the ratio of the input and output beams which is the ratio of the cosines of the internal and external angles.

Appendix B

Fibre electro-optic characterisation using a heterodyne Mach-Zehnder interferometer.

B.1 Introduction

In this appendix we shall describe in detail the heterodyne Mach-Zehnder interferometer used for the electro-optic characterisation of our fibre samples (see chapter 4). The importance of these measurements lies in the fact that the second-order nonlinearity isn't directly measurable in a non-phase-matched SHG process in fibre geometry. It is therefore necessary to measure the electro-optic coefficient r which is related to the effective nonlinear coefficient by the relation

$$r = \frac{4}{n^4} \cdot d \tag{B.1}$$

The most popular method for doing this is putting the fibre sample in one arm of a Mach-Zehnder interferometer and measuring the variation of power output as a function of the voltage applied across the poled region. For clarity, in figure B.1 we reproduce the experimental layout (also shown in chapter 4) developed at Kent University in Canterbury by C. Pannell et al.

B.2 Experimental layout

A He/Ne laser source is used for alignment and launched into one end of a 90/10 splitter. The light from a 1550 nm semiconductor laser ($\sim$ 10 mW) is used for the measurements and is launched into the other end of the 90/10 fibre splitter, whose two outputs represent the upper and lower arm of the interferometer. The choice of

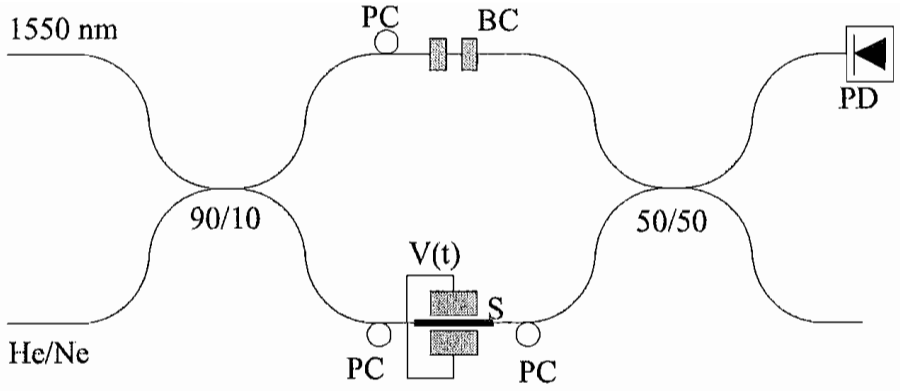

Figure B.1: Experimental layout of the heterodyne Mach-Zehnder interferometer used for our electro-optic measurements. PC - polarisation controller, BC - Bragg cells giving the 50 kHz carrier frequency in the reference arm, He/Ne - visible laser used for alignment, S - fibre sample, PD - photodiode, V(t) - electrodes supplying the sinusoidal voltage, V(t), to the sample.

a 90/10 splitter is based solely on the consideration that the final output must be balanced in power and that the lower arm in which the sample is placed has very high losses (due to coupling into the sample) with respect to the upper arm. In the upper arm a polarisation controller (PC) is followed by two acousto-optic Bragg cells (BC) modulated at 40 MHz. These two cells are placed in such a way as to induce opposite frequency shifts in the optical carrier. By driving the cells at slightly different frequencies it is possible to induce a carrier at a modulation frequency ω_m in the 50 kHz range which can be easily detected with a photodiode (PD) at the output. In the lower arm the fibre sample (S) is placed between two electrodes which provide a modulation signal (V(t)) at frequency Ω and the modulating electric field over a length L of the sample is given by $E(t) = E_m \cos(\Omega t)$. The peak-to-peak voltage is typically in the 100 V range and $\Omega \sim 3 - 5$ kHz. the choice of Ω is rather critical: if the frequency is too low (smaller than 2 kHz) then very strong signals are observed corresponding to mechanical resonances and not to actual electro-optic effects. Light is coupled into and out of the fibre sample using x40 objectives and the polarisation is controlled at both ends with polarisation controllers (PC).

B.3 Theoretical background

It is well known that the output of an interferometer depends on the phase difference accumulated by the light traveling in the two arms. The input propagating electric fields may be written as (using a plane wave approximation)

$$E = 2Ae^{i(\omega t - k_o n_o t)} \tag{B.2}$$

where A is the field amplitude, ω is the field frequency, k_o the corresponding vacuum wave vector and n_o the fibre effective refractive index. The fields passing through

the arms of the interferometer will be modulated so that they become (supposing that the power is perfectly balanced between the two arms)

$$E_{BC} = Ae^{i(\omega t - k_o n_o t - \omega_m t)} \tag{B.3}$$

in the upper arm and

$$E_S = Ae^{i(\omega t - k_o(n_o t + \Delta n))} \tag{B.4}$$

in the lower arm, where Δn is a refractive index change induced in the fibre sample by the electro-optic effect and is given by the relation [8]

$$k\Delta nL = \frac{k_o n^3}{2} r_{33} L E_m \cos(\Omega t) = \phi \cos(\Omega t) \tag{B.5}$$

The total intensity at the output is given by

$$I = |E_{BC} + E_S|^2 = A^2(1 + \cos(\omega_m t - k_o \Delta nL)) \tag{B.6}$$

Putting together equations (B.5) and (B.6) we have

$$I = A^2(1 + \cos(\omega_m t)\cos(\phi\cos(\Omega t)) + \sin(\omega_m t)\sin(\phi\cos(\Omega t))) \tag{B.7}$$

and if $|\phi << 1|$ we have (using some trigonometric identities)

$$I = A^2(1 + \cos(\omega_m t) + \frac{\phi}{2}(\sin(\omega_m + \Omega)t + \sin(\omega_m - \Omega)t)) \tag{B.8}$$

The first term is a DC component, the second is the carrier frequency generated in our experiment by the Bragg cells at 50 kHz and the last term gives the two side-bands induced by the electro-optic modulation in the fibre sample. These frequency components may be visualised and measured with an RF spectrum analyzer. The ratio R of the mean square current generated by the carrier frequency, $< i_c^2 >$, and either one of the sidebands, $< i_{\pm 1}^2 >$, is given by

$$R = \frac{< i_c^2 >}{< i_{\pm 1}^2 >} = \frac{\phi^2}{2} \tag{B.9}$$

and if the difference in dB between the two peaks is defined as ΔI_{dB} then we have

$$\phi = \sqrt{2} \cdot 10^{(\frac{\Delta I_{dB}}{20})} \tag{B.10}$$

or, in terms of the electro-optic coefficient

$$r = \sqrt{2}\frac{n_o^3}{2k_o L E_m} 10^{(\frac{\Delta I_{dB}}{20})} \tag{B.11}$$

By measuring the ratio between the carrier frequency and the sideband peak intensities and using this last equation it is therefore possible to deduce r. A typical measurement, obtained from our thermally poled holey fibres for two different Ω modulating frequencies (3.5 and 4.5 kHz), is shown in figure B.2. In this case, $\Delta I_{dB} \sim 60\ dB$ and $r \sim 0.02\ pm/V$.

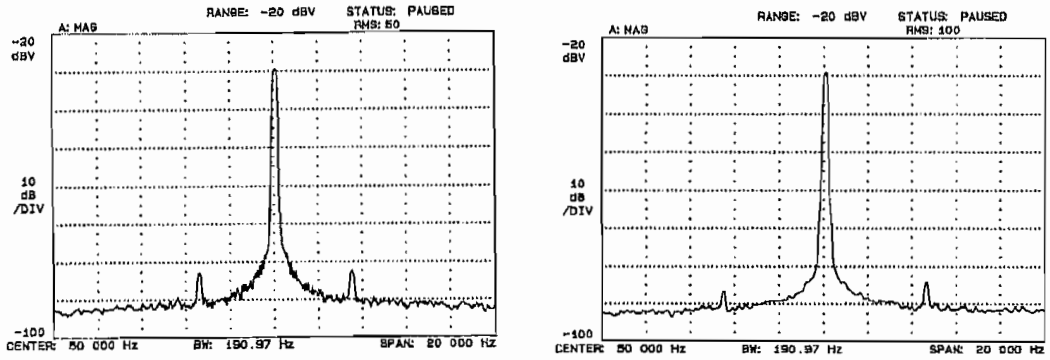

Figure B.2: Images taken from the RF spectrum analyzer showing the sideband peaks for two different modulating frequencies (3.5 and 4.5 kHz).

Appendix C

List of publications

In this appendix a list of the publications and presentations related to this work and to which the author contributed is presented.

Conferences

1. D. Faccio, V. Pruneri, and P.G. Kazansky.
   Two-Beam Noncollinear Makers Fringe Technique.
   CLEOEUROPE 2000, paper CThE29, September 2000

1. D. Faccio, A. Busacca, V. Pruneri, P.G. Kazansky, T.M. Monro, W. Belardi, D.J. Richardson,B. Grappe, M. Cooper, and C.N. Pannell.
   First demonstration of thermal poling in holey fibres
   CLEO2001, Baltimore USA, May 2001

Journal publications

1. D. Faccio, V. Pruneri, and P.G. Kazansky.
   Noncollinear Makers Fringe measurements of second-order nonlinear layers.
   Optics Letters, vol. 25 (18), pp. 1376-1378, September 2000
2. D. Faccio, V. Pruneri, and P.G. Kazansky.
   Dynamics of the second-order nonlinearity dynamics in thermally poled silica glass.
   Submitted to Applied Physics Letters
3. D. Faccio, A. Busacca, D.W.J. Harwood, G. Bonfrate, V. Pruneri, and P.G. Kazansky.
   Effect of core-cladding interface on thermal poling of germano-silicate optical waveguides.
   Submitted to Applied Physics Letters
4. D. Faccio, V. Pruneri, A. Busacca, Rybaltovsky, and P.G. Kazansky.
   Dynamics of the surface potential in thermally-poled silica-glass.
   Submitted to Electronics Letters

5. C. Cabrillo, J.M Gibson, J.A. Johnson, F.J. Bermejo, D. Faccio, V. Pruneri, and P.G. Kazansky.
   Thermally poled silica samples are structurally heterogeneous: electron diffraction evidence of partial crystallization.
   submitted to Applied Physics Letters

Bibliography

[1] S.J.B. Yoo. Wavelength conversion technologies for WDM network applications. *J. Lightwave Tech.*, 14(6):955–966, 1996.

[2] S.J.B. Yoo. US patent 5434700. 1995.

[3] C.Q. Xu, H. Okayama, and M. Kawahara. 1.5 μm band efficient broadband wavelength conversion by difference frequency generation in a periodically domain inverted $LiNbO_3$ channel waveguide. *Appl. Phys. Lett.*, 63:3559, 1993.

[4] E.M. Dianov, P.G. Kazansky, and D. Yu Stepanov. Problem of the photoinduced second harmonic generation. *Sov. J. Quantum Electron*, 19:575, 1989.

[5] R. A. Myers, N. Mukherjee, and S. R. J. Brueck. Large second-order nonlinearity in poled fused silica. *Opt. Lett.*, 16(22):1732–1734, November 1991.

[6] V. Pruneri, G. Bonfrate, P. G. Kazansky, D.J. Richardson, N.G. Broderick, J.P. deSandro, C. Sommineau, P. Vidakovic, and J.A. Levenson. Greater than 20%efficient frequency doubling of 1532 nm nanosecond pulses in quasi-phase-matched germanosilicate fibres. *Opt. Lett.*, 24(4):208–210, 1999.

[7] M.M. Fejer, G.A.Magel, D.H. Jundt, and R.L. Byer. Quasi-phase-matched second harmonic generation: tuning and tolerances. *IEEE J. Quantum Electron.*, 278(11):2631–2654, 1992.

[8] A. Yariv. *Optical Electronics in modern communications.* Oxford University Press, New York, fifth edition, 1997.

[9] B.E.A. Saleh and M.C. Teich. *Fundamentals of photonics.* Wiley, New York, 1991.

[10] R. C. Alferness. Waveguide electro-optic modulators. *IEEE Trans. microwave theory and tech.*, MTT-30(8):1121–1137, 1982.

[11] M. Abe, T.Kitagawa, K. Hattori, A. Himeno, and Y. Ohmori. Electro-optic switch constructed with a poled silica-based waveguide on a Si substrate. *Electron. Lett.*, 32(10):893–894, 1996.

[12] T. Erdogan. Fiber grating spectra. *J. Lightwave Tech.*, 15(8):1277–1294, 1997.

[13] V. Pruneri, G. Bonfrate, and P. G. Kazansky. Efficient frequency doubling of 1.5 μm in quasi-phase-matched optical fibres. *Appl. Phys. Lett.*, 72(9):1007–1009, 1998.

[14] G. Bonfrate, V. Pruneri, P. G. Kazansky, P. Tapster, and J.G. Rarity. Parametric fluorescence in periodically poled silica fibres. *Appl. Phys. Lett.*, 75(16):2356–2358, 1999.

[15] G. Bonfrate. *Optical parametric processes in periodically poled silica fibres.* PhD thesis, University of Southampton, 2000.

[16] H. Imai, S. Horinouchi, N Asakuma, K. Fukao, D. Matsuki, H. Hirashima, and K. Sasaki. Effects of introduction of sodium and water on second order nonlinearity in poled synthetic silica glass. *J. Appl. Phys.*, 84(10):5415–5418, November 1998.

[17] M. Qiu, Y. Takagaki, S. Egawa, T. Mizunami, and R. Vilaseca. Large second-order susceptibility generated in the cathodic face of silica by doping F^- anions. *Opt. Commun.*, 172:97–101, December 1999.

[18] A.C.Liu, M.J.F. Digonnet, G.S. Kino, and E.J. Knystautas. Improved nonlinear coefficient (0.7 pm/V) in silica thermally poled at high voltage and temperature. *Electron. Lett.*, 36:555–556, March 2000.

[19] V. Pruneri, G. Bonfrate, P.G. Kazansky, H. Takebe, K. Morinaga, M. Kohno, K. Kuwasaki, and T. Takeuchi. High second order optical nonlinearities in thermally poled sol-gel silica. *Appl. Phys. Lett.*, 74(18):2578–2580, 1999.

[20] A. Le Calvez, E. Freysz, and A. Ducasse. Experimental study of the origin of the second-order nonlinearities induced in thermally poled fused silica. *Opt. Lett.*, 22(20):1547–1549, October 1997.

[21] D. Pureur, A. C. Liu, M. J. F. Digonnet, and G. S. Kino. Absolute measurement of the second order nonlinearity profile in poled silica. *Opt. Lett.*, 23(8):588–590, April 1998.

[22] Y. Quiquempois, G. Martinelli, P. Dutherage, P.Bernage, P.Niay, and M. Douay. Localisation of the induced second-order nonlinearity within Infrasil and Suprasil thermally poled glasses. *Opt. Commun.*, 176:479–487, April 2000.

[23] D.Faccio, V. Pruneri, and P.G. Kazansky. Noncollinear makers fringe measurements of second-order nonlinear layers. *Opt. Lett.*, 25(18):1376–1378, September 2000.

[24] K. Tanaka, A. Narazaki, K. Hirao, and N. Soga. Optical second harmonic generation in poled MgO-ZnO-TeO_2 and B_2O_3-TeO_2 glasses. *J. Non-Cryst. Sol.*, 203:49–54, 1996.

[25] H. Nasu, K. Kurachi, A. Mito, H. Okamoto, J. Matsuoka, and K. Kamiya. Second harmonic generation from an electrically polarized TiO_2-containing silicate glass. *J. Non-Cryst. Sol.*, 181:83–86, 1995.

[26] K. Tanaka, A. Narazaki, and K. Hirao. Large optical second order nonlinearity of poled WO_3-TeO_2 glass. *Opt. Lett.*, 25(4):251–253, 2000.

[27] M. Qiu, F. Pi, and G. Orriols. The role of lead component in second harmonic generation in lead silica by electron beam irradiation. *Appl. Phys. Lett.*, 73(21):3040–3042, 1998.

[28] J. Arentoft, K Pedersen, S. I. Bozhevolnyi, M. Kristensen, P. Yu, and C. B. Nielsen. Second harmonic imaging of poled silica waveguides. *Appl. Phys. Lett.*, 76(1):25–27, 2000.

[29] J. Arentoft, M. Kristensen, K Pedersen, S. I. Bozhevolnyi, and P. Shi. Poling of silica with silver-containing electrodes. *Electron. Lett.*, 36(19):1635, 2000.

[30] J. Khaled, T. Fujiwara, M. Ohama, and J. Ikushima. Generation of second harmonics in Ge-doped SiO_2 thin films by ultraviolet irradiation under poling electric field. *J. Appl. Phys.*, 87(5):2137–2141, 2000.

[31] D. Wong, W. Xu, S. Fleming, M. Janos, and KM Lo. Frozen-in electrical field in thermally poled fibres. *Optical Fibre Technology*, 5:235–241, 1999.

[32] D. Wong, W. Xu, and S. Fleming. Charge dynamics and distributions in thermally poled silica fibre. In *SPIE conference on optical devices for fibre communcation*, volume 3847, pages 88–92, September 1999.

[33] T. Fujiwara, D. Wong, and S. Fleming. Large electrooptic modulation in a thermally poled germanosilicate fiber. *IEEE Phot. Tech. Lett.*, 7(10):1177–1179, 1995.

[34] T. Fujiwara, M. Takahashi, and A. J Ikushima. Second-harmonic generation in germanosilicate glass poled with ArF-laser irradiation. *Appl. Phys. Lett.*, 71(8):1032–1034, 1997.

[35] M. Nakanishi, O. Sugihara, N. Okamoto, H. Fujimura, and C. Egami. Electron beam irradiation induced nonlinearity in silicate glass films and fabrication of nonlinear optical gratings. *J. Appl. Phys.*, 86(5):2393–2396, 1999.

[36] P. Blazkiewicz, W. Xu, D. Wong, J. Canning, M. Asland, and G.Town. Carbon dioxide laser-assisted poling of silicate-based optical fibres. *Opt. Lett.*, 25(4):200–202, 2000.

[37] V. Pruneri and P.G. Kazansky. Frequency doubling of picosecond pulses in periodically poled D-shaped silica fibre. *Electron. Lett.*, 4(33):318–319, 1997.

[38] P. G. Kazansky, L. Dong, and P.St.J. Russell. High second-order nonlinearities in poled silicate fibres. *Opt. Lett.*, 19(10):701–703, 1994.

[39] P. G. Kazansky et al. Pockels effect in thermally poled silica optical fibres. *Electron. Lett.*, 31(1):62–63, 1995.

[40] V. Pruneri and P. G. Kazansky. Electric-field thermally poled optical fibres for quasi-phase matched second harmonic generation. *IEEE Phot. Tech. Lett.*, 9(2):185–187, 1997.

[41] J. Jerphagnon and K. Kurtz. Maker fringes a detailed comparison of theory and experiment for isotropic and uniaxial crystals. *J. Appl. Phys.*, 41(4):1667–1681, 1970.

[42] P.N. Butcher and D. Cotter. *The elements of nonlinear optics.* Cambridge University Press, Cambridge, 1990.

[43] V. Pruneri, F. Samoggia, G. Bonfrate, P. G. Kazansky, and G. M. Yang. Thermal poling of silica in air and under vacuum: the influence of charge transport on second harmonic generation. *Appl. Phys. Lett.*, 74(17):2423–2425, 1999.

[44] Y. Quiquempois, G. Martinelli, F. Valentin, P. Bernage, P. Niay, and M. Douay. Improved method for measuring second-order nonlinearity profile in poled silica. In *Conference on Bragg gratings, photosensitivity and fibre optics*, ThE21, pages 106–108, September 1999.

[45] N. Bloembergen and P. S. Pershan. Light waves at the boundary of nonlinear media. *Phys. Rev.*, 128:606–622, 1962.

[46] V. Dimitriev, G. Gurzadyan, and D. Nikogosyan. *Handbook of Nonlinear Optical Crystals.* Springer, New York, second edition, 1995.

[47] K.D. Singer, M.G. Kuzyuk, and J.E. Sohn. Second-order nonlinear-optical processes in orientationally orderd materials: relationship between molecular and macroscopic properties. *J. Opt. Soc. Am. B*, 4(6):968–976, 1987.

[48] S. Kielich. Optical second harmonic generation by electrically polarized isotropic media. *IEEE J. Quantum Electron.*, QE-5(12):562–568, 1969.

[49] B.F. Levine and C.G. Bethea. Second and third order hyperpolarizabilities of organic molecules. *The Journal of Chem. Phys.*, 63(6):2666–2682, 1975.

[50] G.H. Chartier, P. Jassaud, A.D. Oliveira, and O. Parriaux. Optical waveguides fabricated by electric-field controlled ion exhange in glass. *Electron. Lett.*, 14(5):132–134, 1978.

[51] S. Batchelor, R. Oven, and D.G. Ashworth. Characterisation of electric field assisted diffused potassium ion planar optical waveguides. *Electron. Lett.*, 32(22):2082–2083, 1996.

[52] N.J. Chou and J.M. Eldridge. Effects of material and processing parameters on the dilectric strength of thermally grown SiO_2 films. *JAP*, 117(10):1287–1293, 1970.

[53] K. Tanaka, Y. Miyamoto, M. Itoh, and E. Bychkov. Ionic conduction in glasses. *Phys. Stat. Sol. (a)*, 173:317–323, 1999.

[54] H. Kahnt. Ionic transport in glasses. *J. Non-Cryst. Sol.*, 203:225–231, 1996.

[55] P.G. Kazansky and P. St. J. Russell. Thermally poled glass: frozen-in electric field or oriented dipoles? *Opt. Commun.*, 110:611–614, 1994.

[56] N. Okamoto, Y. Hirano, and O. Sugihara. Precise estimation of nonlinear-optical coefficients for anisotropic nonlinear films with $C_{\infty v}$ symmetry. *J. Opt. Soc. Am. B*, 9(11):2083–2087, November 1992.

[57] T. G. Alley, S. R. J. Brueck, and M. Wiedenbeck. Secondary ion mass spectrometry study of space charge formation in thermally poled fused silica. *J. Appl. Phys.*, 86(12):6634–6640, 1999.

[58] T. G. Alley, S. R. J. Brueck, and R. A. Myers. Space charge dynamics in thermally poled fused silica. *J. Non-Cryst. Sol.*, 242:165–176, 1998.

[59] A. von Hippel. Photocurrent, space-charge buildup and field emission in alkali halide crystals. *Phys. Rev.*, 91(3):568–579, August 1953.

[60] U. K. Krieger and W. A. Lanford. Field assisted transport of Na ions, Ca ions and electrons in commercial soda-lime glass. *J. Non-Cryst. Sol.*, 102:50–61, 1988.

[61] W. A. Lanford, K. Davis, P. Lamarche, R. Groleau, and R. H. Doremus. Hydration of soda-lime silica glass. *J. Non-Cryst. Sol.*, 33:249–266, 1979.

[62] G. Hetherington, K. H. Jack, and M. W. Ramsay. The high-temperature electroysis of vitreous silica. *Phys. Chem. Glasses*, 6(1):6–12, 1965.

[63] P.J. Jorgensen and F.J. Norton. Proton transport during hydrogen permeation in vitreous silica. *Phys. Chem. Glasses*, 10(1):23–27, 1969.

[64] W.T. Lynch. Calculation of electric field breakdown in quartz as determined by dielectric dispersion analysis. *J. Electrochem. Soc.*, 43(8):3274–3278, 1972.

[65] John Chubb Instrumentation. *http://www.jci.co.uk.*

[66] P.G. Kazansky, A. R. Smith, P. St. J. Russell, G. M. Yang, and G. M. Sessler. Thermally poled silica glass: laser induced pressure pulse probe of charge distribution. *Appl. Phys. Lett.*, 68(2):701–703, 1996.

[67] T.A. Birks, J.C. Knight, and P. St. J. Russell. Endlessly single-mode photonic crystal fibre. *Opt. Lett.*, 22(13):961–963, 1997.

[68] T.M. Monro, D.J. Richardson, N.G.R. Broderick, and P.J. Bennett. Holey optical fibres: an efficient modal model. *J. Lightwave Tech.*, 16:923–928, 1999.

[69] M. Qiu, F. Pi, G. Orriols, and M. Bibiche. Signal damping of second harmonic generation in poled soda-lime silicate glass. *J. Opt. Soc. Am. B*, 15(4):1362–1365, April 1998.

[70] R. A. Myers, X. Long, and S. R. J. Brueck. Recent advances in the second-order nonlinear optical properties of amorphous silica materials. *Doped fibers, devices and systems SPIE*, 2289, July 1994.